

Transmission of an ICME sheath into the Earth's magnetosheath and the occurrence of traveling foreshocks

Matti Ala-Lahti¹, Andrew P. Dimmock², Tuija I. Pulkkinen^{3,4},
Simon W. Good¹, Emilyya Yordanova², Lucile Turc¹, and Emilia K. J. Kilpua¹

¹Department of Physics, P.O. Box 64, University of Helsinki, Helsinki, Finland

²Swedish Institute of Space Physics, Uppsala, Sweden

³Department of Climate and Space Sciences and Engineering, University of Michigan, Ann Arbor, MI,
USA

⁴Department of Electronics and Nanoengineering Engineering, Aalto University, Espoo, Finland

Key Points:

- Several intervals in an ICME sheath maintained their magnetic structure with transmission into the Earth's magnetosheath
- The intervals caused traveling foreshocks, ultralow-frequency fluctuations, and back-streaming ions upstream of the quasi-parallel bow shock
- Correlation of observations from a solar wind monitor and a spacecraft in the magnetosheath depends on spacecraft alignment

Corresponding author: Matti Ala-Lahti, matti.ala-lahti@helsinki.fi

This is the author manuscript accepted for publication and has undergone full peer review but has not been through the copyediting, typesetting, pagination and proofreading process, which may lead to differences between this version and the [Version of Record](#). Please cite this article as [doi: 10.1029/2021JA029896](https://doi.org/10.1029/2021JA029896).

This article is protected by copyright. All rights reserved.

Abstract

The transmission of a sheath region driven by an interplanetary coronal mass ejection into the Earth's magnetosheath is studied by investigating in situ magnetic field measurements upstream and downstream of the bow shock during an ICME sheath passage on May 15, 2005. We observe three distinct intervals in the immediate upstream region that included a southward magnetic field component and are traveling foreshocks. These traveling foreshocks were observed in the quasi-parallel bow shock that hosted backstreaming ions and magnetic fluctuations at ultralow frequencies. The intervals constituting traveling foreshocks in the upstream survive transmission to the Earth's magnetosheath, where their magnetic field, and particularly the southward component, was significantly amplified. Our results further suggest that the magnetic field fluctuations embedded in an ICME sheath may survive the transmission if their frequency is below ~ 0.01 Hz. Although one of the identified intervals was coherent, extending across the ICME sheath and being long-lived, predicting ICME sheath magnetic fields that may transmit to the Earth's magnetosheath from the upstream at L1 observations has ambiguity. This can result from the strong spatial variability of the ICME sheath fields in the longitudinal direction, or alternatively from the ICME sheath fields developing substantially within the short time it takes the plasma to propagate from L1 to the bow shock. This study demonstrates the complex interplay ICME sheaths have with the Earth's magnetosphere when passing by the planet.

1 Introduction

Interplanetary coronal mass ejections (ICMEs) are massive clouds of plasma and magnetic field that originate from vast eruptions in the Sun's corona. They transfer energy in interplanetary space and are the main drivers of space weather at the Earth (e.g., Gonzalez et al., 1999, 2011; Kilpua et al., 2017a, and references therein). An ICME consists of a magnetic ejecta which drives a shock and sheath region when traveling with supermagnetosonic speeds relative to the solar wind in interplanetary space. Interplanetary shocks, including those not associated with ICMEs, have been extensively studied (e.g., Tsurutani et al., 2011; Blanco-Cano et al., 2016; Oliveira & Samsonov, 2018; Kajdič et al., 2019). And several recent works have focused on understanding the radial evolution of ICME ejecta (e.g., Manchester et al., 2017; Scolini et al., 2018; Good et al., 2019; Janvier et al., 2019; Lugaz et al., 2020; Luhmann et al., 2020) and the sheath regions driven by ICMEs (e.g., Yermolaev et al., 2018; Moissard et al., 2019; Good et al., 2020; Salman et al., 2020). New missions, such as Solar Orbiter (Müller et al., 2013) and Parker Solar Probe (Fox et al., 2016), can improve the understanding of ICMEs by observing them closer to the Sun and earlier in their evolution (see e.g., Winslow et al., 2021).

Each of these elements of the ICME have an independent capability to disturb the plasma environments that surround the Earth (e.g., Tsurutani et al., 1988; Zhou & Tsurutani, 2001; Huttunen et al., 2002; Pulkkinen et al., 2007; Yermolaev et al., 2012). ICME sheaths have a vital contribution to most severe geomagnetic storms (Huttunen & Koskinen, 2004; Kilpua et al., 2017a; Meng et al., 2019) and they can drive intense substorms (Tsurutani et al., 2015). An ICME sheath passage through the Earth's magnetosphere compresses the dayside magnetopause (e.g., Lugaz et al., 2016) and causes strong auroral currents in the high-latitude magnetosphere (Huttunen et al., 2002; Huttunen & Koskinen, 2004) and large geomagnetically induced currents (Huttunen et al., 2008; Dimmock et al., 2019). In addition, intense low-energy particle precipitation to the upper atmosphere (Knipp et al., 2013) and depletion of relativistic electrons fluxes in the outer Van Allen radiation belts (e.g., Hietala et al., 2014; Turner et al., 2019) can occur due to the sheath passage.

The importance of ICME sheaths to space weather results from their high dynamic pressure and southward magnetic fields (see e.g., Burton et al., 1975; Crooker, 2000; Boudouridis et al., 2005; Lindsay et al., 1995; Kilpua et al., 2019). The key mechanisms generating southward fields in the sheath are shock compression of pre-existing out-of-ecliptic fields in the

70 solar wind, turbulence downstream of an interplanetary shock, and field line draping of the
71 interplanetary magnetic field (IMF) around the driving ejecta (Tsurutani et al., 1988; Lugaz
72 et al., 2016). Improved space weather predictions require a comprehensive understanding of
73 the interplay between the ICME and the Earth’s magnetosphere, and the ability to deter-
74 mine these southward fields within the ICME sheaths (Tsurutani et al., 2020). Moreover,
75 spatial variability of sheath fields in the longitudinal direction at 1 AU and its consequences
76 for space weather has been addressed by Ala-Lahti et al. (2020). The ICME sheath fields
77 have a large-scale structure being more coherently structured compared to the solar wind.
78 They, however, also host local and spatially limited magnetic fluctuations, the space weather
79 impact being thus dependent on the magnetic fine structure of the ICME sheath (see also
80 Good et al., 2020). Discrete magnetic field discontinuities embedded in an ICME sheath
81 can cause abrupt compression of the dayside magnetosphere and excite wave generation in
82 the inner magnetosphere (Blum et al., 2021).

83 Direct observations of the interaction between an ICME sheath and the Earth’s mag-
84 netosphere, including the transmission of an ICME sheath into the Earth’s magnetosheath,
85 are important for constructing a thorough picture of the interaction. A dominant process for
86 geomagnetic disturbances is dayside magnetic reconnection requiring a southward field in
87 the magnetosheath. This is typically from the southward IMF but can also be locally south-
88 ward from magnetosheath transients such as high speed jets (Nykyri et al., 2019). Therefore,
89 we need a complete understanding of how the various structures inside the ICME sheath
90 interact with the dayside magnetosphere since they can possibly dictate the field direction
91 at the dayside magnetopause.

92 In this study, we examine the sheath region of the ICME on May 13, 2005. The ICME
93 and its impact on the Earth’s magnetosheath have been previously studied (e.g., Dasso et
94 al., 2009; Yurchyshyn et al., 2006; Bisi et al., 2010; Turc et al., 2014). The impact of the
95 ICME ejecta on the Earth’s magnetosheath has also been investigated statistically (Turc
96 et al., 2017). The ICME-driven sheath region was observed at 1 AU on May 15, 2005, first
97 by the ACE and Wind spacecraft in the upstream solar wind, subsequently by the Cluster
98 spacecraft, and finally by the Geotail spacecraft in the Earth’s magnetosheath. We investi-
99 gate the occurrence of magnetic structures and fluctuations embedded in the ICME sheath
100 that were transmitted, across the Earth’s bow shock and into the magnetosheath. With
101 transmit we refer to magnetic field features and properties in the bow shock downstream
102 region, which were observable already in the upstream. We also examine if the upstream
103 magnetic field fluctuation frequency affects how well the structures maintain their charac-
104 teristics across the shock. The location of Cluster, in the immediate upstream of the bow
105 shock during the event, constitutes the frame of reference in this study. We focus on the
106 southward component of the transmitted structures, while considering the overall dynamics
107 of the bow shock during the ICME sheath – magnetosheath encounter.

108 The study is constructed as follows. Section 2 introduces the range of spacecraft obser-
109 vations during the ICME event at 1 AU on May 15, 2005. Section 3 focuses on the magnetic
110 field within the ICME sheath that is transmitted to the Earth’s magnetosphere, and the
111 spatial and temporal extent of the identified magnetic structures. Section 4 discusses the
112 relation of the observations to bow shock dynamics. Section 5 concludes with discussion.

113 2 Observations

114 Magnetic field data with a resolution of 10.9 Hz from Wind (Lepping et al., 1995), 1 Hz
115 from ACE (Smith et al., 1998), 22.4 Hz from Cluster (Balogh et al., 1997) and 16 Hz from
116 Geotail (Kokubun et al., 1994) are analyzed in this study. We also present and analyze
117 data from the Wind Solar Wind Experiment (Ogilvie et al., 1995), from the ACE Solar
118 Wind Electron Proton Alpha Monitor (SWEPAM; McComas et al., 1998), from the Cluster
119 Ion Spectrometry (CIS) Experiment (Réme et al., 1997), and from the Geotail Low Energy
120 Particle (LEP) Experiment (Mukai et al., 1994).

Figure 1a–c show the spacecraft locations and the global ICME observations at 1 AU on May 15, 2005 in Geocentric Solar Ecliptic (GSE) coordinates. The panels present a sketch of the magnetopause (black) and bow shock (red) boundaries during the sheath passage, with the trajectories of the Cluster 3 and Geotail spacecraft shown for 01:00–06:00 UT and Fig. 1c having a cut-out of the GSE x -axis. ACE and Wind, both in the proximity of L1, had a relatively large longitudinal separation during the event, ACE being close to the Sun–Earth line and Wind at about $90 R_E$ duskward. The change in location of ACE and Wind during the observation time period was negligible. The GSE y -separation between ACE and Cluster 3 (Geotail) was between 15 and $20 R_E$ (14 – $19 R_E$). Between Wind and Cluster 3 (Geotail), the separation varied from 98 to $103 R_E$ (from 97 to $102 R_E$). The insert in Fig. 1a also illustrates the magnetosheath boundaries during nominal solar wind conditions preceding the ICME (dashed curves). It can be seen that the ICME sheath compressed the magnetosheath resulting in the Cluster 3 spacecraft entering from the magnetosheath into the bow shock upstream region. Geotail was located in the magnetosheath flank during the entire ICME sheath passage apart from short visits in the bow shock upstream region between $\sim 05:13$ – $05:15$ UT and $\sim 05:36$ – $05:41$ UT, initially quite far downstream from the point where Cluster 3 exited the magnetosheath. In this study, ‘upstream’ refers to Cluster 3 observing the ICME sheath prior to its interaction with the bow shock and magnetosheath, and ‘downstream’ refers to the Geotail observations in the magnetosheath during the ICME passage. Geotail traveled towards the bow shock during the event and the separation with Cluster decreased during the course of the event.

Figure 1d–g and h–k show the magnetic field (B), plasma speed (V) and proton density (n) measurements from ACE and Wind during the event. The ICME sheath is bounded by the red vertical lines. ACE and Wind observed the interplanetary shock at 02:11 and 02:13 UT, and the ejecta leading edge at 05:30 and 05:31 UT, respectively. The measurements display strong fluctuations of both magnetic field magnitude and its components, and significant variations in plasma parameters, all characteristic features of an ICME sheath region (e.g., Kilpua et al., 2017b). The driving ICME ejecta is clearly noticeable from the smooth rotating magnetic field.

Figure 2 focuses on magnetic field measurements during the ICME sheath crossing. We have resampled the magnetic field data to 1 Hz resolution, the highest resolution available for all four spacecraft. Panels (a–d) are sorted according to the GSE y -component of the spacecraft position at the beginning of the event, with Wind measurements at the top and Geotail (GT) measurements at the bottom. The measurements are time-shifted so that the arrival time of the ICME sheath, marked by the red dashed vertical line, coincides at all spacecraft. The arrival time at Cluster 3 (C3), 02:38:45 UT on May 15, 2005, is used as the reference time, the used time-shifts being 25 min 45 s, 27 min 35 s and -20 s, for Wind, ACE and GT, respectively. Upon inspecting the simultaneous ICME sheath and magnetosheath observations, there are common structures observed in both datasets with remarkable similarities. The goal of the study is to understand the physical nature of how these magnetosheath structures arise. Three intervals of interest labeled 1–3 are highlighted with pink dotted rectangles in Fig. 2c. Selected data from these intervals are shown at smaller scales in the right-hand panels in Fig. 2e–l, with corresponding labels 1–3 and interval 1 augmented with plasma observations in Fig. 2g and h.

At C3, interval 1 spans the arrival of the ICME and the exit of the spacecraft from the Earth’s magnetosheath. In Fig. 2c, it can be seen in interval 1 that there were fluctuations with relatively large amplitude and similar magnetic field magnitudes ($|B|$) before and after the sheath arrival time. C3 was in the magnetosheath before the ICME encountered the magnetosphere, as indicated by the $|B|$ values of 25 – 30 nT and proton densities of ~ 25 cm $^{-3}$ before the arrival of the sheath, which are much higher values than those observed in the solar wind before the sheath arrival at L1. The sheath arrival at C3 is manifested by the enhancement of the magnetic field magnitude and increases of n and V . The plasma speed gradually increased until C3 exited the magnetosheath at 02:39:22 UT, the exit being also

174 indicated by a drop in $|B|$ and n . The C3 magnetosheath exit is marked by the black dashed
 175 vertical line in the interval 1 in Fig. 2e and g. Data from the equivalent interval at GT show
 176 that the beginning of the event is defined by an abrupt increase of $|B|$.

177 Three intervals with notable southward field components can be distinguished with
 178 visual inspection of the C3 measurements in Fig. 2c. They are also distinct at GT and occur
 179 in the same chronological order at both spacecraft, suggesting that at least part of their
 180 properties were preserved as they transmitted from the upstream into the magnetosheath.
 181 These intervals are marked by the second and third rectangles (i.e., intervals 2 and 3) in
 182 Fig. 2c and are highlighted in the corresponding right-hand panels in Fig. 2i–l. The C3 and
 183 GT spacecraft made these observations with longitudinal separations of $0.3 R_E$ and $4.8 R_E$,
 184 respectively. During these three intervals the magnetic field fluctuated substantially, and
 185 the out-of-ecliptic component, B_z , in the upstream at C3 had average values of -4.8 , -9.1
 186 and -11.8 nT, in chronological order. The average was 5.3 nT elsewhere in the sheath.
 187 Corresponding B_z values in the magnetosheath at GT during the ICME sheath passage were
 188 -16.8 , -38.0 and -34.8 , and 14.0 nT, respectively. The values of $|B|$ were also enhanced
 189 during these intervals (C3: 28.2 , 29.9 and 26.0 , and 17.7 nT; GT: 58.2 , 58.0 and 63.2 , and
 190 43.4 nT). We will investigate these intervals in more detail below.

191 In addition, all spacecraft observed prominent large-scale field variations at the back of
 192 the ICME sheath, the boundary between the ICME sheath and ejecta being marked by red
 193 dashed lines at $\sim 06:00$ UT. The duration of the sheath passage is slightly longer at C3 and
 194 GT than at Wind and ACE.

195 3 Correlation Analysis

196 We compute the Pearson correlation coefficients for the magnetic field measurements
 197 in the intervals that, according to the previous visual investigation, were transmitted to the
 198 Earth's magnetosphere during the ICME sheath passage on May 15, 2005. We also investi-
 199 gate how the transmission of ICME sheath magnetic fields may depend on the frequency
 200 of the field fluctuations, and whether the transmitted field features were long-lasting occur-
 201 rences in the ICME sheath prior to encountering the magnetosphere. The first 37 s of the
 202 ICME sheath interval at C3, when the spacecraft was still within the magnetosheath, are
 203 excluded from the analysis by marking the ICME sheath beginning at C3 at $02:39:22$ UT
 204 (see the black dashed vertical line in Fig. 2e).

205 Similar to Ala-Lahti et al. (2020), we compute the total Pearson correlation by applying
 206 the averaging estimator of correlation coefficients (Olkin & Pratt, 1958) for the individual
 207 Pearson correlation coefficients of the magnetic field magnitude and components. Pearson
 208 correlation coefficient measures the linear dependence of two random variables and is used to
 209 compare spacecraft measurements (e.g., Good et al., 2018; Lugaz et al., 2018). The overall
 210 or total correlation is defined as

$$211 \sigma_{tot} = \frac{\sum_{i=1}^4 (n_i - 1)}{\sum_{i=1}^4 (n_i - 4)} \left[\sigma_{P,i} + \frac{\sigma_{P,i}(1 - \sigma_{P,i}^2)}{2(n_i - 3)} \right], \quad (1)$$

212 where i refers to the magnetic field magnitude or component, $\sigma_{P,i}$ is the corresponding
 213 Pearson correlation coefficient, and n is the size of the sample (Alexander, 1990; Ala-Lahti
 et al., 2020).

214 We compute σ_{tot} for the C3 and GT data for the identified three intervals in order to
 215 quantify the visual similarity at the two spacecraft. We select the intervals in the upstream
 216 (C3) as follows: (1) $02:59:29 - 03:04:39$ UT, (2) $03:10:03 - 03:13:49$ UT, and (3) $05:28:09 -$
 217 $05:35:49$; and hereafter refer to these intervals as 'structures' in the magnetic field. The
 218 boundaries are based on a number of features in the magnetic field observations in the
 219 upstream, such as abrupt changes in the magnitude or orientation of the magnetic field, or

220 the onset or ending of significant fluctuations. All the structures were convected by the bulk
 221 flow, checked by performing the timing analysis (Paschmann & Daly, 1998; Eastwood et al.,
 222 2005b) using data from all four Cluster spacecraft.

223 In order to have well-defined correlation coefficients that account for distinguishable
 224 features of the structures, we have to consider longer intervals than the ones defined by
 225 the three structures. We note that the definitions of the structure boundaries include some
 226 degree of subjectivity. We control this subjectivity by varying the duration of the structure
 227 intervals when computing σ_{tot} . Furthermore, we examine the characteristics of the structures
 228 at L1 (ACE and Wind).

229 Figure 3a–c show C3 data, with the structure boundaries marked by gray dashed vertical
 230 lines. Panels (d–l) show GT, ACE and Wind data. The magnetic field data shown in each
 231 plot are aligned relative to the beginning of the sheath arrival at C3 (02:39:22 UT shown in
 232 Fig. 2). The spacecraft data is resampled to 1 Hz.

233 The intervals bounded by the blue solid vertical lines in Fig. 3a–c demarcate intervals
 234 ± 3 min of the structure boundaries. These extended C3 intervals are cross-correlated with
 235 the data at GT, ACE and Wind shown in Fig. 3d–l, with σ_{tot} calculated at each step of
 236 the cross-correlation. The resulting series of σ_{tot} values are given in Fig. 3m–o. The σ_{tot}
 237 time series show the correlation at each time step, with the investigated GT, ACE or Wind
 238 intervals being centered at the time step. The maxima of the σ_{tot} cross-correlations are
 239 indicated by stars for each series, with the maxima values listed at the bottom right corners
 240 of the panels. Pale solid vertical lines in Fig. 3d–l indicate the data intervals that give the
 241 maxima in σ_{tot} . The analysis is defective for structure (3) at Wind because of a data gap.

242 In addition to the extended ± 3 min intervals, we repeat the above analysis by consid-
 243 ering the structures with ± 1.5 – 4.5 min extensions in steps of 30 s. We also consider the
 244 spacecraft data resampled to 0.5, 0.2 and 0.1 Hz. Figure 3p–r show the locations of maxi-
 245 mum correlation, similar to the stars in Fig. 3m–o. Different markers indicate the resampling
 246 resolution used but they do not distinguish different interval lengths used in our analysis.

247 The correlation analysis presented in Fig. 3 suggests that the structures in the upstream,
 248 i.e., in the C3 data, were transmitted to the magnetosheath and observed by GT. The
 249 intervals identified by the correlation analysis, marked by the pairs of pale vertical lines in
 250 Fig. 3d–f, coincide with the previous visual inspection of the data. Furthermore, the analysis
 251 presented in Fig. 3p–r indicates that the identification is robust: the position of maximum
 252 correlation does not depend on the resampling resolution or on the precise length of the
 253 interval centered on the structure. This is indicated by the stable position of the green
 254 markers, and it applies for all three upstream structures. We note that as the duration of
 255 the structure remains much greater than the resampling resolutions, the σ_{tot} values increase
 256 as resampling resolution decreases due to the lower resampling resolution smoothing out the
 257 high frequency fluctuations observed within the structures.

258 The comparison of structures (1) and (2) at C3 with the observations at ACE and Wind
 259 gives lower σ_{tot} maxima than with GT (Fig. 3g–f, j–k and m–n), which may result from the
 260 spacecraft at L1 having a different cross-section through the structures. The times giving
 261 maximum σ_{tot} also vary depending on the resampling resolution and interval length used
 262 (Fig. 3p and q). Moreover, the same interval at Wind is identified as the most probable
 263 candidate for both structures (1) and (2) in the correlation analysis. The same appears
 264 also for ACE to some extent, when considering Fig. 3m–n and p–q. Visual inspection on
 265 the other hand suggests that the intervals centered at $\sim 02:55$ UT at ACE and at Wind
 266 correspond to each other in Fig. 3g and j. The intervals marked by the vertical lines in
 267 Fig. 3h and k also exhibit visual similarity.

268 The occurrence of structures (1) and (2) at L1 is further investigated by studying them
 269 together. Similar to the analysis above, an interval bounded by the beginning of structure (1)
 270 (the first gray dashed line in Fig. 3a) and the ending of structure (2) (the second gray dashed

line Fig. 3b) is compared to the ACE and Wind data. The intervals giving the maximum correlations are marked by the gray solid lines in Fig. 3h and k, and the corresponding σ_{tot} values given by the upward and downward pointing triangles for ACE and Wind in Fig. 3n, respectively. The purple triangles in Fig. 3q, which do not differentiate different resampling resolutions, indicate a robust identification at ACE. The teal triangles for the comparison with the Wind data are more scattered and indicate relatively small correlation.

This is consistent with the findings reported by Ala-Lahti et al. (2020), namely that magnetic fluctuations in ICME sheaths exhibit spatial structuring with heliospheric longitude at 1 AU. This can explain the ambiguity in identifying structures (1) and (2) at L1, especially at Wind, which had a relatively large longitudinal spacecraft separation with C3 during the observation time period (Section 2 and Fig. 1a–c). However, the combined identification of structures (1) and (2) at ACE implies the structures had a larger than 15 R_E longitudinal width, a conclusion not possible from the comparison of the data from C3 and GT. In addition, some structures evidently are large-scale and spatially coherent across the ICME sheath and sufficiently long-lasting, such as structure (3), which is robustly identified by the correlation analysis at ACE and by eye at both ACE and Wind (see Fig. 3), and the prominent large-scale field variations at the back of the ICME sheath.

Alternatively, the magnetic fields of an ICME sheath may develop substantially while traveling from L1 to the Earth. Consequently, observations at L1 would not always be sufficient to forecast, for example, strong southward magnetic fields in the Earth’s magnetosheath, such as those seen in structures (1) and (2).

We extend the above analysis for the whole ICME sheath on May 15, 2005 to examine how the identified structures compare to other magnetic field features during the event. We compare 10 min C3 intervals resampled at 1 Hz to intervals at GT. A 10 min interval is comparable in duration to the intervals indicated by the blue vertical lines in Fig. 3. Again the spacecraft measurements are aligned using the sheath arrival time as reference, and we compare a C3 interval to a set of GT intervals similarly as in Fig. 3. The results for the cross-correlation of the C3 intervals with the time-shifted GT data are shown in Fig. 4a, where the time on the horizontal axis gives the center of the C3 interval in question, and where the lag on the vertical axis gives the difference in time between the centers of the C3 and GT intervals analyzed. The red dashed lines indicate the beginning and end of the ICME sheath event and the black dotted lines indicate the intervals given by the blue lines in Fig. 3. The corresponding analysis for time-shifted ACE and Wind is shown in Fig. 4b and c, respectively.

Consistent with our previous results, Fig. 4a highlights structures (1)–(3) (bounded by the black dotted lines) and their surroundings with relatively higher values of σ_{tot} . In addition, the map suggests that the structures were not sole ‘survivors’ in the transmission of the ICME sheath to the Earth’s magnetosheath. The map distinguishes patches of relatively high correlation between \sim 03:20 and 04:20 UT. These correspondences in the field features in the upstream (C3) and downstream (Geotail) are also evident from visual inspection of the timeseries (see Fig. 2c and d). During the period at \sim 03:25–03:37 UT, B_z was positive and B_x and B_y negative, with the interval ending at a sharp polarity reversal of the magnetic field direction. During \sim 04:05–04:15 UT, the field components experienced a polarity reversal, B_z (B_x and B_y) being at first negative (positive). The magnetic field in the upstream additionally experienced a gradual rotation at \sim 03:46–03:52 UT, which is not observable by eye in Fig. 2 but which appears in Fig. 4a as a patch of high correlation. We note that, contrary to the structures (1)–(3), the intervals discussed here do not have noteworthy southward B_z (see Fig. 2c and d).

In particular, structures (2) and (3) are discernible in terms of patches that indicate a considerable correlation in Fig. 4b for ACE. The same applies for structure (1) to some extent. Figure 4c for Wind shows only weak associations for structures (1) and (2), but there is a period of high correlation at the back of the sheath at both spacecraft. The

323 better correlations with ACE can depend on the GSE y location of the spacecraft (see
 324 Fig. 1). This implies spatial variability in ICME sheaths, with the spacecraft location being
 325 sensitive to detecting different features in the magnetic fields. The back of the ICME
 326 sheath after structure (3) exhibits a well-correlated period at all spacecraft, corresponding to
 327 visually discernible large-scale field variations. The panels do not display significant patches
 328 elsewhere in the ICME sheath. These observations are in agreement with our analysis in
 329 Fig. 2 and 3.

330 We complete our correlation analysis by examining the dependence of the transmission
 331 of upstream ICME sheath magnetic fields into the Earth's magnetosheath on the frequency
 332 of the field fluctuations. First, we define two thresholds for σ_{tot} . We construct a distribution
 333 of σ_{tot} values by taking the maximum value at each point in time during the ICME sheath
 334 passage in Fig. 4a, i.e., the maximum correlation across the lag range at each time. The
 335 median and upper quartiles of the resulting σ_{tot} distribution are 0.48 and 0.60. The lower
 336 quartile of the distribution is $\sigma_{tot} \simeq 0.30$ and set as the lower limit of the color bars in Fig. 4.
 337 Next, we band-pass filter the C3 and GT magnetic field data, compute σ_{tot} values similar
 338 to those in Fig. 3, construct the distribution of the maximum correlations and compute the
 339 percentage of the distribution above the thresholds defined above. We examine ten bands
 340 with frequency ranges defined by $\beta \cdot 10^\alpha$ Hz, where β is equal to 1.0-2.5, 2.5-5.0, 5.0-7.5
 341 and 7.5-10.0 Hz, and α varies from -3 to -1; the two highest β ranges are excluded when
 342 $\alpha = -1$, giving ten bands in total. We also vary the length of the investigated intervals from
 343 the 10 min used earlier, computing in addition σ_{tot} for 5, 20 and 30 min C3 data intervals.

344 The patches in Fig. 5a coincide with the intervals identified and discussed previously;
 345 within a given patch, the color denotes the highest frequency range for which there is good
 346 correlation (i.e., $\sigma_{tot} \geq UQ$). In addition, the highest frequency band given in the figure
 347 shows multiple patches with different lags for a given time. This may result from wave-like
 348 features prevailing in the frequency band, with waves having a different phase between the
 349 locations in upstream and downstream where the observations were made. The analysis
 350 for all frequency bands, interval lengths and both correlation thresholds is summarised in
 351 Fig. 5b, which shows the percentage of the band-pass-filtered σ_{tot} distribution above a given
 352 threshold (0.48 or 0.60) as a function of frequency. The legend indicates whether only 10 min
 353 or all data interval lengths are considered. In the latter case, the average of percentages
 354 across the four different interval lengths is computed. Additionally, the legend indicates
 355 the threshold used (given in brackets). The horizontal error bars in the figure show the
 356 frequency bands for other than the highest frequencies where they would overlap.

357 Figure 5b gives an indication of the frequency dependence of the transmission of mag-
 358 netic fluctuations from the ICME sheath into the Earth's magnetosheath. We note our
 359 analysis is limited, for example due to changes in spacecraft position and a relative large
 360 spacecraft separation that restrict the subsequent observations of short-lived small-scale
 361 fluctuations. However, larger-scale fluctuations in ICME sheath exhibit less spatial vari-
 362 ability (Ala-Lahti et al., 2020) and the results presented in Fig. 5 are an indicative of a
 363 trend. The figure shows that the probability of feature transmission increases significantly
 364 for frequencies below ~ 0.01 Hz. This finding is in agreement with Rakhmanova et al. (2015),
 365 who reported similar frequency ranges when examining solar wind origin magnetic fluctu-
 366 ations in the Earth's magnetosheath. They concluded that bow shock and magnetosheath
 367 processes contribute considerably to the distribution of magnetic fluctuations at higher fre-
 368 quencies. Furthermore, they suggested that higher-frequency magnetic fluctuations might
 369 also enter the magnetosheath if embedded in dense solar wind with large $|B|$. ICME sheaths
 370 are solar wind transients which typically exhibit both of these conditions (e.g., Kilpua et
 371 al., 2017b). However, the increase in probability in Fig. 5 occurs only at frequencies below
 372 ~ 0.01 Hz, possibly due to the limitations noted above. We further discuss the transmission
 373 of higher-frequency fluctuations in the next section, because waves at higher frequencies in
 374 the upstream are thought to transmit to the downstream (e.g., Clausen et al., 2009; Villante
 375 et al., 2011; Francia et al., 2012; Takahashi et al., 2021).

376 We conclude that magnetic structures (1)-(3) embedded in the ICME sheath observed
 377 on May 15, 2005 were transmitted into the Earth's magnetosheath. They are detectable
 378 in the spacecraft data by visual inspection and stand out in our correlation analysis. The
 379 structures differed from other discernible intervals in the correlation analysis due to their
 380 southward field components, which were notably amplified when transmitted into the Earth's
 381 magnetosheath. There is, however, ambiguity as to whether these structures were present
 382 further upstream at L1. Not all fluctuations appearing in the upstream did survive the
 383 transmission into the downstream, only lower-frequency fluctuations transmitting into the
 384 magnetosheath.

385 4 Bow Shock Dynamics – Traveling Foreshocks

386 We here continue the examination of structures (1)-(3) by relating them to the bow
 387 shock dynamics. We have estimated the bow shock angle, defined as the angle between
 388 the shock normal and upstream magnetic field direction (θ_{Bn}), by following the field lines
 389 given by the C3 measurements during the ICME sheath passage and by modeling the bow
 390 shock using the model by Merka et al. (2005). This estimation is compared to the particle
 391 energy flux of the sunward traveling ions measured by the C3 CIS instrument. The C3
 392 measurements and estimated bow shock angle during the event are presented in Fig. 6,
 393 where black dotted vertical lines mark the structure boundaries. In Fig. 6c, which shows
 394 the bow shock angle θ_{Bn} , the solid gray curve gives the angle along the upstream field lines
 395 while the dashed one gives the estimation during periods when the field lines did not connect
 396 to the bow shock, the angle being then estimated along the straight radial path from the
 397 spacecraft to the Earth.

398 Figure 6 indicates that, during the event, C3 frequently observed fluxes of sunward
 399 traveling ions, which correspond to ions reflected from the bow shock, and which are an
 400 observational characteristic of a foreshock upstream of the bow shock (e.g., Eastwood et al.,
 401 2005a). The observed sunward fluxes were coincident with the upstream magnetic field lines
 402 encountering the bow shock, as demonstrated by the solid gray curve. Sunward traveling
 403 (or backstreaming) ions have been previously observed for $\theta_{Bn} \leq 70^\circ$ (e.g., Eastwood et
 404 al., 2005a). Moreover, the shock angle varied considerably and rapidly during the sheath
 405 passage. During the structures identified in this study, the bow shock was quasi-parallel
 406 ($\theta_{Bn} < 45^\circ$), the structure boundaries being associated with abrupt changes of θ_{Bn} . Fluxes
 407 of backstreaming ions were additionally observed during all three structures, which suggests
 408 that the structures constituted transient foreshocks. With a transient foreshock we refer to
 409 a temporary change in the bow shock geometry during which similar magnetic and plasma
 410 phenomena occur in the upstream region that are observed for the global foreshock during
 411 nominal solar wind conditions (see e.g., Kajdič et al., 2017).

412 To examine further whether the structures constituted transient foreshocks, we study
 413 the occurrence of ultralow-frequency (ULF) fluctuations and ion distributions within the
 414 structures. ULF fluctuations from 1 mHz to 1 Hz are regularly observed in the Earth's ion
 415 foreshock (e.g., Burgess, 1997; Eastwood et al., 2005b; Hobara et al., 2007; Wilson, 2016),
 416 and can also be replicated in numerical simulations (e.g., Lin & Wang, 2005; Blanco-Cano
 417 et al., 2006; Turc et al., 2018). They are generated through plasma instabilities, such as
 418 the left-hand resonant ion beam instability (Gary, 1985), which excites fluctuations around
 419 a frequency of 0.1 Hz (a period of 10 s), or the ion-ion beam right-hand instability (Gary,
 420 1991) responsible for generating 30 s fluctuations. These plasma instabilities are triggered
 421 by the interactions between backstreaming ions and the incoming solar wind (e.g., Eastwood
 422 et al., 2003, 2005a; Wilson, 2016).

423 The 30 s ULF fluctuations have been extensively examined (e.g., Greenstadt et al.,
 424 1968; Hsieh & Shue, 2013; Palmroth et al., 2015; Turc et al., 2018), their wave periods
 425 actually ranging from 10 to ~ 55 s depending on the solar wind conditions (Eastwood et al.,
 426 2005b). Initially transverse fluctuations may develop a significant compressive component

427 (Kis et al., 2004; Blanco-Cano et al., 2006; Omidi et al., 2009; Rojas-Castillo et al., 2013;
 428 Kajdič et al., 2017). Moreover, ULF fluctuations in the Earth's ion foreshock often coin-
 429 cide with intermediate, gyrating or gyrophase-bunched ion distributions (Paschmann et al.,
 430 1979; Fuselier, 1995; Eastwood et al., 2005b). Gyrophase bunching implies a distribution
 431 with nonzero mean velocity component perpendicular to the field direction (Fuselier, 1995;
 432 Mazelle et al., 2003). Recent studies have shown that when the IMF strength is large (as
 433 is the case during ICMEs and their sheath regions), the foreshock can exhibit anomalous
 434 features, with in particular the coexistence of 30 s waves at different frequencies, which may
 435 be due to coincident multiple ion beams (Turc et al., 2018, 2019). Wavelet power spectra
 436 can be used to characterize foreshock wave activity.

437 Fig. 7 shows the magnetic field measurements at C3 for structures (1)-(3) in panels
 438 (a-c) and the Morlet wavelet power spectra for parallel (B_{\parallel}) and perpendicular (B_{\perp}) fluctu-
 439 ations with respect to the mean magnetic field direction within the structures in panels
 440 (d-f) and (g-i), respectively. The B_{\parallel} and B_{\perp} components are defined similarly to Moissard
 441 et al. (2019), the perpendicular unit vectors defined as $\mathbf{b}_{1,\perp} = (\mathbf{e}_j \times \mathbf{B}_0)/|\mathbf{e}_j \times \mathbf{B}_0|$ and
 442 $\mathbf{b}_{2,\perp} = (\mathbf{B}_0 \times (\mathbf{e}_j \times \mathbf{B}_0))/(|\mathbf{B}_0 \times \mathbf{e}_j \times \mathbf{B}_0|)$ where \mathbf{e}_j is chosen from the GSE unit vectors
 443 so that the quantity $|\mathbf{e}_j \times \mathbf{B}_0|$ is maximised, \mathbf{B}_0 being the background magnetic field.
 444 The vertical axis indicates the fluctuation period in seconds. In addition, reduced two-
 445 dimensional velocity distribution functions (VDF) in the plasma rest frame in the (V_{\parallel}, V_{\perp})
 446 plane for the structures are shown in Fig. 8. The distribution functions are integrated over
 447 the second perpendicular direction, with the arrows indicating the bulk direction of the
 448 magnetic field and plasma velocity during the structures.

449 Substantially enhanced power in both parallel and perpendicular fluctuations with pe-
 450 riods from 10 to 55 s was found within structures (1) and (2) relative to the surrounding
 451 field (Fig. 7d-e and g-h). High power also appeared at shorter periods. For structure (3),
 452 the same applies for perpendicular fluctuations (Fig. 7i), whereas compressive fluctuation
 453 power, while considerable, was not distinguishable from the surroundings (Fig. 7f). Higher
 454 power at shorter periods is in agreement with previous ULF wave observations: their fre-
 455 quency is roughly proportional to $|B|$ (Hoppe & Russell, 1982; Turc et al., 2019), which
 456 is relatively large for the compressed plasma of ICME sheaths. In addition, Fig. 8, where
 457 the core plasma is indicated by the large values of the phase space density at the proxim-
 458 ity of the centers of the plots, reveals that the two-dimensional VDFs span an extensive
 459 region of phase space. The VDFs in particular occupy the bottom-left quadrants implying
 460 gyrophase-bunched distributions. The distributions in Fig. 8 resemble the disrupted cap
 461 distributions seen in numerical simulations where ULF waves are present, which result from
 462 backstreaming ions interacting with ULF waves (Kempf et al., 2015).

463 The C3 observations within the structures do not unambiguously exhibit all standard
 464 signatures of a foreshock, such as $|B|$, V and n having smaller values in the foreshock than
 465 in the upstream solar wind (see e.g., Kajdič et al., 2017). Relative to the surroundings,
 466 proton density went up in structure (1) and down in (2), plasma speed decreased in both
 467 structure (1) and (2), while density and speed did not change in structure (3) (not shown).
 468 The magnetic field magnitude was also higher than their surroundings within all structures.
 469 However, an antisunward convected solar wind region, which is bounded by rotational dis-
 470 continuities in the IMF that temporarily change a portion of the bow shock geometry to
 471 quasi-parallel and hosts ULF fluctuations and suprathermal ions, causes so-called traveling
 472 foreshock (Kajdič et al., 2017). There were indeed significant changes in field direction at
 473 the structure boundaries, with the bow shock becoming quasi-parallel. In addition, the
 474 structures occurred in conjunction with notable fluxes of sunward traveling (backstreaming)
 475 ions, enhanced power in fluctuations in the 10–55 s period range, and complicated VDFs
 476 manifesting gyrating beams. Thus, we conclude that these structures caused traveling fore-
 477 shocks, during which a transient foreshock occurs upstream of the Earth's bow shock due
 478 to a temporary change in the IMF direction. Due to the close separation of the four Cluster
 479 spacecraft, we cannot compute the spatial scale of these traveling foreshocks and how local

they were (Pfau-Kempf et al., 2016) nor confirm the observation by Kajdič et al. (2017) that the temporal sequence of entry and exit of a traveling foreshock is similar in multiple spacecraft.

To extend the analysis of Section 3 about the transmission of different fluctuations, the wavelet power in the upstream at C3 shown in Fig. 7 is compared to the power in the downstream at GT shown in Fig. 9. Compressive and perpendicular fluctuations in Fig. 9d–f and in Fig. 9g–i, respectively, are computed with respect to the mean field direction within the structures in the upstream. Structures (1) and (3) are discernible in Fig. 9d and g and in Fig. 9f and i, respectively, which show a significant power within the presumable correspondents of the structures at GT (Fig. 9a and c). Structure (2) on the other hand is not as distinguishable from the surrounding field in Fig. 9b and e. However, for all structures (1)–(3), a large power observed for longer fluctuation periods at C3 in Fig. 7 occurred also in the downstream, and in general the power increased from C3 to GT. The wavelet power was also enhanced for shorter fluctuation periods in the downstream.

For completeness, we plot the wavelet power spectra for the entire ICME sheath passage on May 15, 2005 (Fig. 10), which shows the wavelet power of magnetic field magnitude and out-of-ecliptic component for all spacecraft used in this study. The black dashed (dotted) vertical lines delineate the sheath (structure) boundaries and the black solid curves show the proton cyclotron frequency. The power of $|B|$ and B_z both increased from the upstream to the downstream across a wide range of periods through the entire ICME sheath interval. The structures are discernible in the C3 and GT B_z spectra. Similar observations are made for the B_x and B_y components as for B_z (not shown). It is notable that the highest power of B_z is observed just behind the preceding shock and just in front of the ICME leading edge, consistent with the statistical study by Kilpua et al. (2013). These parts of the sheath are key regions for substorms and geoeffectiveness (Kilpua et al., 2019; Kalliokoski et al., 2020). This high power of B_z was also detected by ACE and Wind further upstream at L1.

5 Discussion

In this study we have examined the transmission of structures in an ICME sheath to the Earth’s magnetosheath. We focused on the ICME sheath interacting with the magnetosphere on May 15, 2005, that of the driving ejecta having been previously studied by Turc et al. (2014). We paid particular attention to three intervals in the ICME sheath that transmitted from the immediate upstream of the bow shock to the downstream during the ICME sheath passage maintaining their structure. These intervals, labeled structures (1)–(3), caused traveling foreshocks and were the focus of this study. The structures contained highly southward field component in the upstream region that was amplified significantly in the downstream propagation, increasing their geoeffectiveness. Large amplitude magnetic field fluctuations were present in the structures in both upstream and downstream. Wavelet power in the ULF band and the occurrence of backstreaming ions were examined at the times coinciding with the traveling foreshock structures, and showed intensification especially at higher frequencies as they traveled downstream.

The correlation analysis constructed in this study was in agreement with visual investigation of the spacecraft data, and the identification of the structures in the immediate upstream and downstream was unambiguous. Further in the upstream, in the proximity of L1, the identification of structures (1) and (2) became ambiguous, the ambiguity diminishing at ACE in an additional analysis thus being larger at Wind, which was further away from the Sun–Earth line. On the other hand, a solid identification of structure (3) was made also at L1. Although a large-scale, relatively coherent background magnetic field is embedded in ICME sheaths at 1 AU, they also host local and spatially limited magnetic fluctuations (Ala-Lahti et al., 2020). Our findings are in agreement with this conclusion, especially if structures (1) and (2) were local but steady, long-lived structures already present further upstream. Consequently, the chosen solar wind monitor is important when studying the

531 interaction of an ICME sheath with the Earth's magnetosheath. An alternative is that the
532 magnetic field fluctuation properties of ICME sheaths can change relatively quickly with
533 time (i.e. during the propagation time between the spacecraft), even in a manner that is
534 expected to have implications for their space weather response.

535 Moreover, although our analysis implies that the structures were limited in the lon-
536 gitudinal direction, their extent might have been comparable to the width of the Earth's
537 magnetosheath in the GSE y and z directions. This is consistent with the identification of
538 the structures at ACE data but not at Wind. In such a case, the bow shock angle would
539 differ from the one given in Fig.6 depending on the position in the upstream. Thus, the
540 transmission of the structures into the Earth's magnetosheath might vary along the bow
541 shock due to varying shock configuration and dynamics, which could result in an even more
542 localized occurrence of the structures in the downstream. Our analysis indeed demonstrated
543 that the bow shock angle can experience abrupt changes and quickly adjust to the upstream
544 magnetic field. We showed here that the reaction of the magnetosheath to the upstream
545 field changes is almost immediate. During structures (1) - (3), the bow shock was in addition
546 quasi-parallel and the structures constituted traveling foreshocks. Although some upstream
547 magnetic fields correlated with the observations in the downstream when the bow shock
548 was quasi-perpendicular, the studied ICME sheath passage had considerable intervals, such
549 as at $\sim 04:30-05:00$, when no significant correlations were observed between upstream and
550 downstream measurements.

551 As a consequence of the varying shock dynamics, space weather effects in the inner
552 magnetosphere may be very complicated during an ICME sheath passage. This applies
553 especially for interactions between the magnetopause and southward fields embedded in an
554 ICME sheath, such as structures (1) - (3) investigated in this study. Magnetic structures in
555 an ICME sheath can indeed excite localised wave generation in the inner magnetosphere
556 (Blum et al., 2021). The above scenario can occur for steady, long-living magnetic structures
557 and for magnetic structures/fluctuations generated while an ICME sheath propagates from
558 L1 to the bow shock.

559 We found that the probability of the upstream magnetic fields surviving the transmis-
560 sion to the Earth's magnetosheath during the ICME sheath passage was dependent on the
561 frequency of the magnetic fluctuations. Our analysis showed that surviving the transmis-
562 sion became more probable when fluctuations had frequencies below ~ 0.01 Hz. This is in
563 agreement with previous research (Rakhmanova et al., 2015). We note, however, that waves
564 at higher frequencies are thought to transmit across the bow shock (e.g., Clausen et al.,
565 2009; Takahashi et al., 2021) and more observations are needed for further conclusions.

566 The traveling foreshocks included fluctuations with periods in the ULF range. These
567 waves were possibly generated by the backstreaming ions in the traveling foreshocks. The
568 lower levels of magnetic fluctuations further in the upstream at L1 is in agreement with this
569 conclusion (assuming the occurrence of the structures already at L1).

570 The transmission of the ULF fluctuations was not extensively investigated in this study.
571 However, an enhanced wavelet power was observed within structures (1) - (3) at ULF wave
572 periods in the upstream and downstream, with a larger power in the downstream that also
573 extended to shorter fluctuation periods. Foreshock ULF waves are considered to be a sig-
574 nificant source of magnetospheric fluctuations (Takahashi et al., 1984), which may reach
575 the inner magnetosphere (Russell et al., 1983; Villante et al., 2011; Francia et al., 2012).
576 From this perspective, the magnetic field configurations embedded in ICME sheath fields
577 that form traveling foreshocks and excite the generation of ULF waves result in a complex
578 interplay between an ICME sheath and the Earth's magnetosheath: All fluctuations trans-
579 mitted from the upstream to the magnetosheath during an ICME sheath passage are not
580 necessarily fluctuations that originated from the solar wind. Instead, an ICME sheath pas-
581 sage may result in bow shock dynamics that generate foreshock ULF waves, which are then
582 transmitted into the magnetosheath. Together with pre-existing ICME sheath fluctuations,

583 the generated ULF waves may constitute foreshock turbulence, which can lead to magne-
584 topause reconnection (Chen et al., 2021), thus compounding the space weather impact of
585 the ICME sheath.

586 The complex interplay together with spacecraft locations may actually explain the
587 low correlation at higher frequencies in Fig. 5. As discussed above, longitudinally (and
588 latitudinally) extended structures that are observed in the upstream, such as structures
589 (1)-(3), modify the shock configuration. Because of this and of the shock curvature, their
590 interaction with the shock, and a possible foreshock, will vary with space and time. In
591 addition, fluctuations within them may evolve due to the dynamics of the ICME sheath
592 itself, or that of the traveling foreshock, before the structures enter the downstream. For
593 example, ULF fluctuations excited within a structure entering the magnetosheath flank
594 have more time to develop a compressive component than if the structure crossed the bow
595 shock closer to the Sun-Earth line. ULF waves within a lasting foreshock region can further
596 deepen, forming shocklets and short-large-amplitude magnetic structures (e.g., Kajdič et
597 al., 2017, and references therein). Foreshock waves have also a shorter longitudinal extent
598 when present inside a driver, which has higher $|B|$ than more typical solar wind (Archer
599 et al., 2005; Turc et al., 2018, 2019). Consequently, fluctuations at higher frequencies
600 can differ substantially from each other between the upstream observation location and
601 their bow shock crossing location that precedes their subsequent downstream observation
602 location, whereas extended larger-scale structures may be preserved from the upstream to
603 the downstream being observed by spacecraft that are not radially aligned. This scenario
604 is applicable for the entire ICME sheath passage, during which the spacecraft separation
605 in the GSE yz -plane between C3 and GT varied between 6.5 and 7.5 R_E . In addition, the
606 magnetosheath dynamics during the ICME sheath passage could have modified fluctuations
607 properties at higher frequencies during the traveling time from C3 to GT, which had a
608 spacecraft separation in the GSE x -direction between 1.0 and 4.6 R_E during the event.

609 Finally, structures (1)-(2) might have originated from magnetic field fluctuations pre-
610 existing in the solar wind that were swept by the ICME sheath (see e.g., Tsurutani et
611 al., 1988). Such pre-existing fluctuations experience shock compression twice: first when
612 entering the ICME sheath and second when the ICME sheath transmits to the Earth's
613 magnetosheath. Alternatively, the structures could have been generated by the in-situ
614 dynamics of the turbulent plasma downstream of an interplanetary shock. The downstream
615 turbulence is dependent on conditions in the preceding solar wind (see e.g., Pitňa et al., 2016,
616 2021; Zank et al., 2021). These scenarios also emphasize the importance of understanding
617 the dynamics of the solar wind. Successive observations of the same ICME sheath by
618 multiple spacecraft with relatively small separations would improve our understanding of
619 these origins. Solar Orbiter and Parker Solar Probe will provide opportunities to investigate
620 if these structures are present closer to the Sun.

621 Structure (3) and the coinciding large-scale field variations at the back of the ICME
622 sheath observed by all spacecraft could have emanated from field line draping around the
623 driving ejecta (e.g., Gosling & McComas, 1987; Tsurutani et al., 1988; McComas et al.,
624 1989). As discussed by Jones et al. (2002), the orientations of the constituent magnetic
625 fields accreting at the back of the ICME sheath should remain tangential to the local leading
626 surface of the driving ejecta. This accretion can form periods of organized layers of magnetic
627 fields known as planar magnetic structures (Nakagawa et al., 1989). The occurrence of
628 planar magnetic structures in the ICME sheath observed at 1 AU on May 15, 2005 was
629 investigated by Palmerio et al. (2016), and interestingly, the authors reported a planar
630 magnetic structure only in the mid-sheath. We note that the identification was performed
631 with Wind data, which had a significant data gap during structure (3), and that deviations
632 from the general field line draping pattern can occur (Kaymaz & Siscoe, 2006). Large-scale
633 field variations at the back of the ICME sheath can also result from the erosion of the ICME
634 ejecta (Dasso et al., 2006; Ruffenach et al., 2012; Lavraud et al., 2014; Manchester et al.,
635 2014).

636 ICME sheaths and their interplay with the Earth's magnetosphere constitute an in-
637 triguing coupled system. We highlight, together with the work by Ala-Lahti et al. (2020)
638 and by Blum et al. (2021), the importance that the fine structure of sheath fields have in
639 this interplay. Predicting ICME sheath structures and properties that are relevant for space
640 weather and geoefficiency can be particularly challenging due to the complex dynamics of
641 ICME sheaths, which can vary with propagation from the Sun. The magnetic fine structure
642 observed at L1 might not always match reality at the Earth due to the spacecraft location
643 or due to the evolution of the fluctuations. This is important for space weather predictions
644 that are dependent on observations at L1.

Acknowledgments

ACE and Wind data used in this study are available at the NASA Goddard Space Flight Center Coordinated Data Analysis Web (CDAWeb, <http://cdaweb.gsfc.nasa.gov/>). The investigated magnetic field (plasma) data were measured by the ACE and Wind Magnetic Fields Investigation (ACE Solar Wind Electron Proton Alpha Monitor and Wind Solar Wind Experiment) instruments. The ACE and Wind data sources and their documentation are given by California Institute of Technology (<http://www.srl.caltech.edu/ACE/>) and NASA (<https://wind.nasa.gov/data.php>).

Cluster data analyzed in this study were obtained from the Cluster Science Archive (<https://csa.esac.esa.int/csa-web/>). Magnetic field (plasma) data from the Cluster Fluxgate Magnetometer (Ion Spectrometry) instrument were investigated. The Cluster data sources and their documentation are given by ESA (<https://www.cosmos.esa.int/web/csa/>).

Geotail data analyzed in this study were obtained from Data ARchives and Transmission System (DARTS), provided by Center for Science-satellite Operation and Data Archive (C-SODA) at ISAS/JAXA (<https://darts.isas.jaxa.jp/stp/geotail/data>). Magnetic field (plasma) data from the Geotail Magnetic Field Experiment (Low Energy Particle Experiment) instruments were investigated. The Geotail data sources and their documentation are given by DARTS (<https://darts.isas.jaxa.jp/stp/geotail/>).

We thank the sources for providing data. MA-L, EK, SWG and LT acknowledge The Finnish Centre of Excellence in Research of Sustainable Space, funded through the Academy of Finland Grant 312390. MA-L, EK and SWG also acknowledge Academy of Finland Project 310445 (SMASH). This project has received funding from the European Research Council (ERC) under the European Union's Horizon 2020 research and innovation program (grant agreement 724391, SolMAG). APD received financial support from the Swedish National Space Agency (grant 2020-00111). The work by TP is supported by Academy of Finland grant 310444 and NSF grant 2033563. EY research was funded by the Swedish Civil Contingencies Agency (grant 2016-2021) and SNSA (grant 86/20). The work of LT is supported by the Academy of Finland (grant number 322544) and the University of Helsinki (three-year research grant 2020-2022).

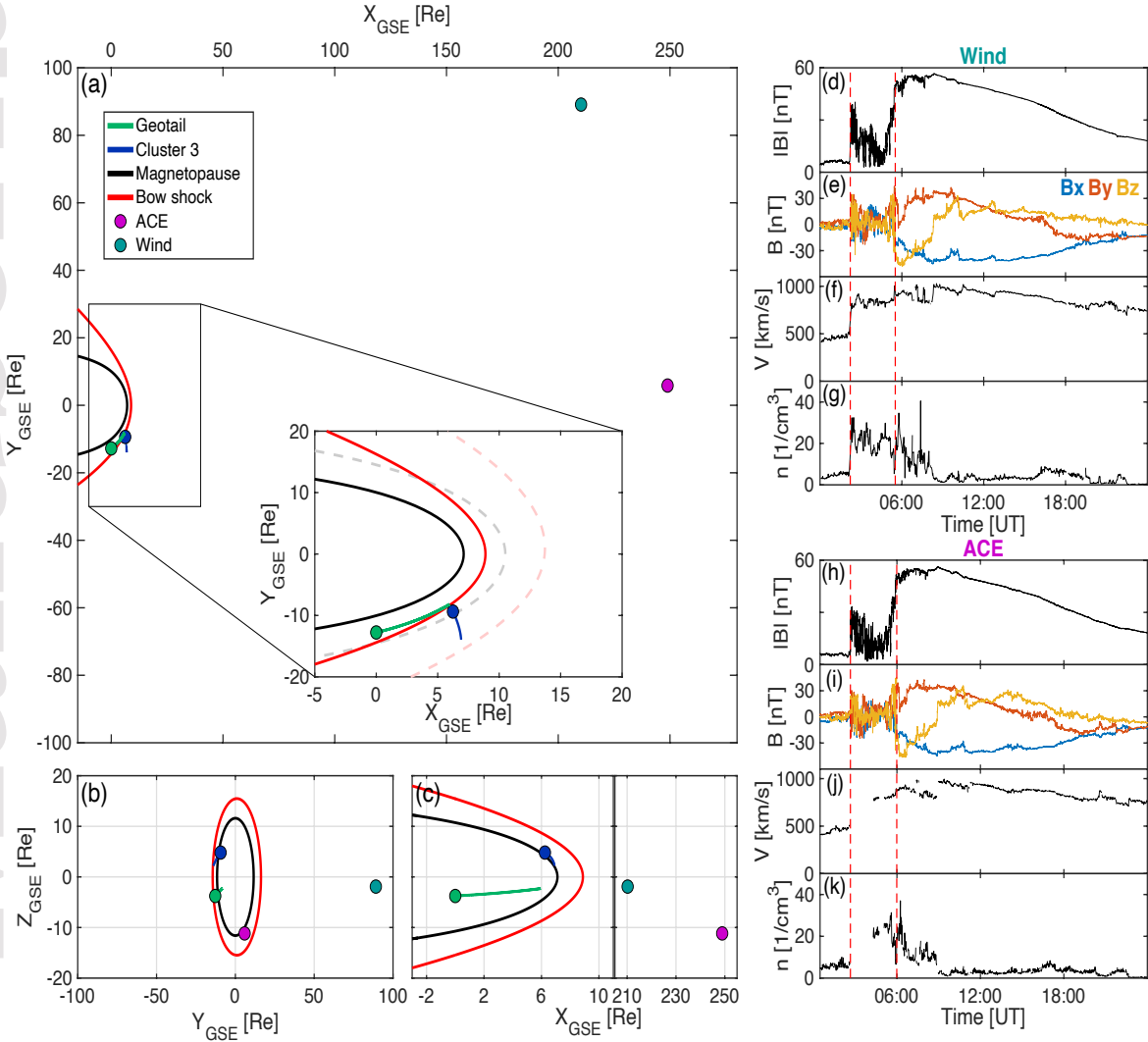


Figure 1. (a–c) Sketch of near-Earth space in Geocentric Solar Ecliptic (GSE) coordinates at 01:00–06:00 UT on May 15, 2005 showing the trajectories of the Geotail (green) and Cluster 3 (blue) spacecraft, and the mean positions of the ACE (purple) and Wind (teal) spacecraft. The change in position for ACE and Wind was negligible in this time period, unlike for Geotail and Cluster 3. Earth’s magnetopause (solid black lines) and bow shock (solid red lines) are modeled during the ICME sheath passage using Wind measurements (Shue et al., 1998; Merka et al., 2005). Dashed lines in panel (a) indicate the magnetosheath boundaries for the solar wind conditions prior to the ICME arrival. There is a cut-out of the GSE x-axis in panel (c). (d–g) Magnetic field magnitude ($|B|$), magnetic field components (B), speed (V), and proton density (n) measured by Wind and (h–k) ACE on May 15, 2005. Vertical red dashed lines indicate the times of the interplanetary shock preceding the ICME sheath (ACE 02:11 UT; Wind: 02:13 UT) and the leading edge of the driving ICME (ACE: 05:30 UT; Wind: 05:31 UT).

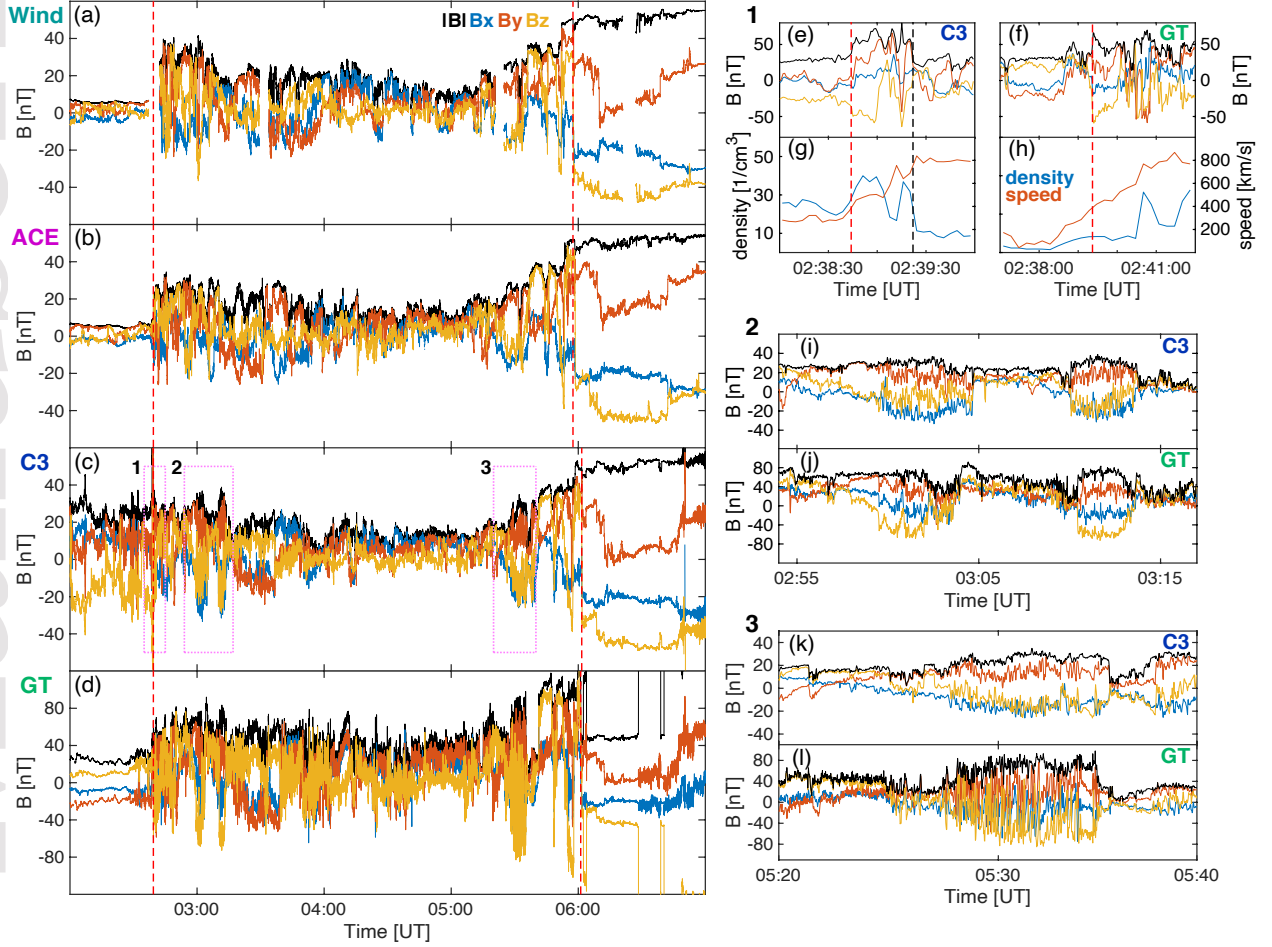


Figure 2. (a–d) Magnetic field measurements from Wind, ACE, Cluster 3 (C3) and Geotail (GT) during the ICME-driven sheath region on May 15, 2005, at 1 Hz resolution. The measurements are time-shifted and aligned relative to the beginning of the event at C3 (dashed red lines). The pink boxes in panel (c) indicate three intervals of interest, as follows: (1) the beginning and arrival of the ICME sheath indicated by a fast forward interplanetary shock, and (2 and 3) sub-structures in the C3 data, which have a notable negative out-of-ecliptic component and that also appear in the Geotail data. The dashed red lines at $\sim 06:00$ UT indicate the trailing edge of the sheath i.e., the leading edge of the driving ICME ejecta. Selected data from the three intervals are shown in panels (e–l). The magnetosheath exit of C3 is marked by the black dashed line. Proton density and plasma speed are shown for the interval 1 in panels (g–h).

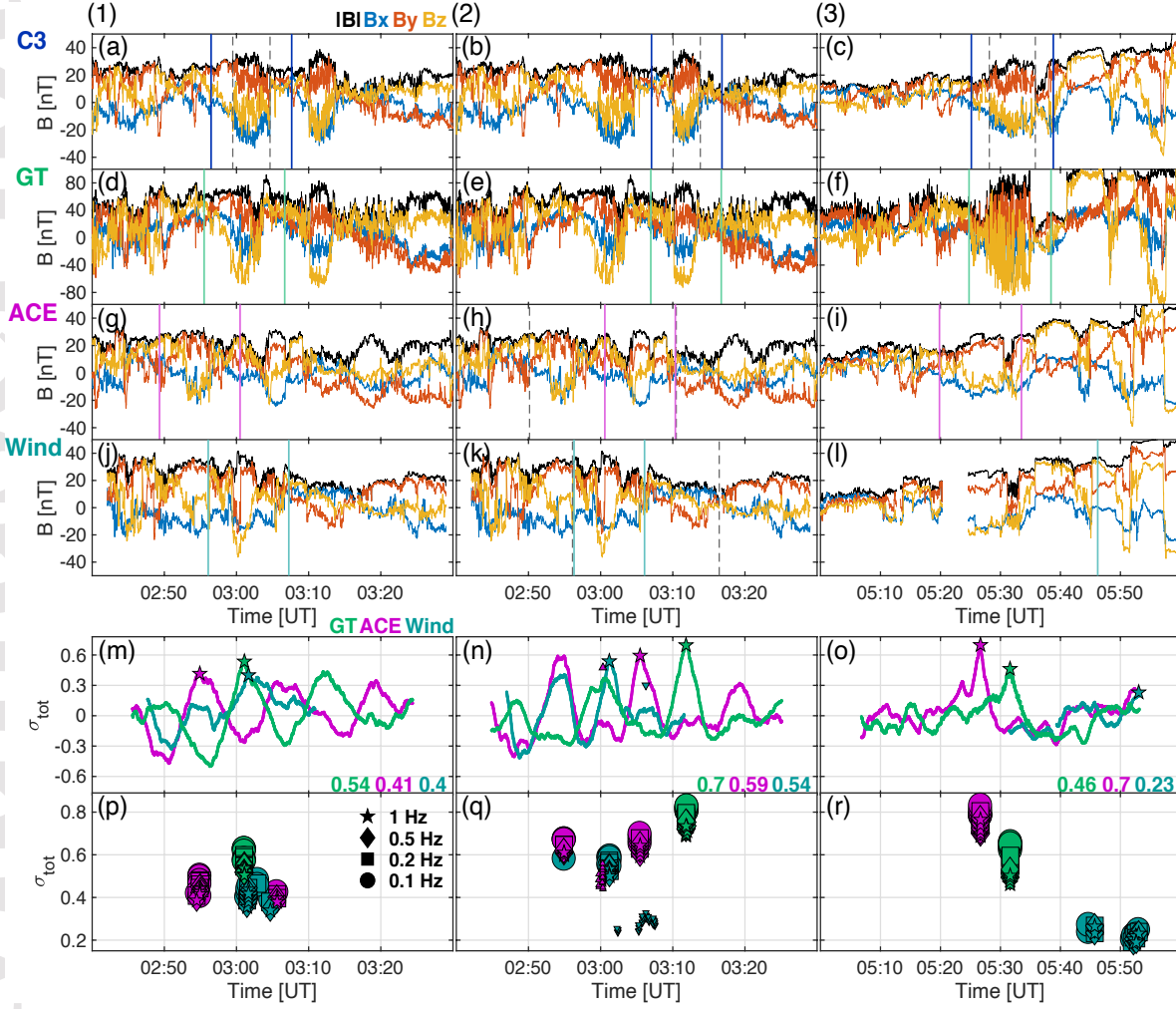


Figure 3. Correlation coefficient analysis comparing the correspondence of Geotail, ACE and Wind magnetic field data to a sub-interval of C3 data defined by boundaries marked with blue vertical lines in panels (a–c). Columns 1–3 correspond to structures (1)–(3), respectively. (a–l) The magnetic field data of the spacecraft. (m–o) The total cross-correlation (σ_{tot}) of the sub-interval given in panels (a–c) with the data at the other spacecraft. Correlation values were calculated for sub-intervals at the other spacecraft with durations equal to that of the corresponding C3 interval. Correlation values at the mid-point of the sliding intervals are shown in panels (m–o). Peak values in the cross-correlation are indicated by stars and corresponding numerical values given in the bottom right corners of panels (m–o). Panels (p–r) show how the location of these highest correlations vary when the boundaries marked by the blue vertical lines in panels (a–c) vary and when data are resampled to lower resolutions (to 0.5, 0.2 and 0.1 Hz). The boundaries in panels (p–r) vary from 1:30 min to 4:30 min in steps of 30 s, the addition of 3 min representing the middle value of this vector. The gray dashed lines in panels (h) and (k) indicate the intervals corresponding the peak values marked by an upward and downward pointing triangles in panel (n), when structures (1) and (2) are considered together at ACE and Wind, respectively. The triangles in panel (q) show how the location of these highest correlations vary when the data resolution and interval length are varied.

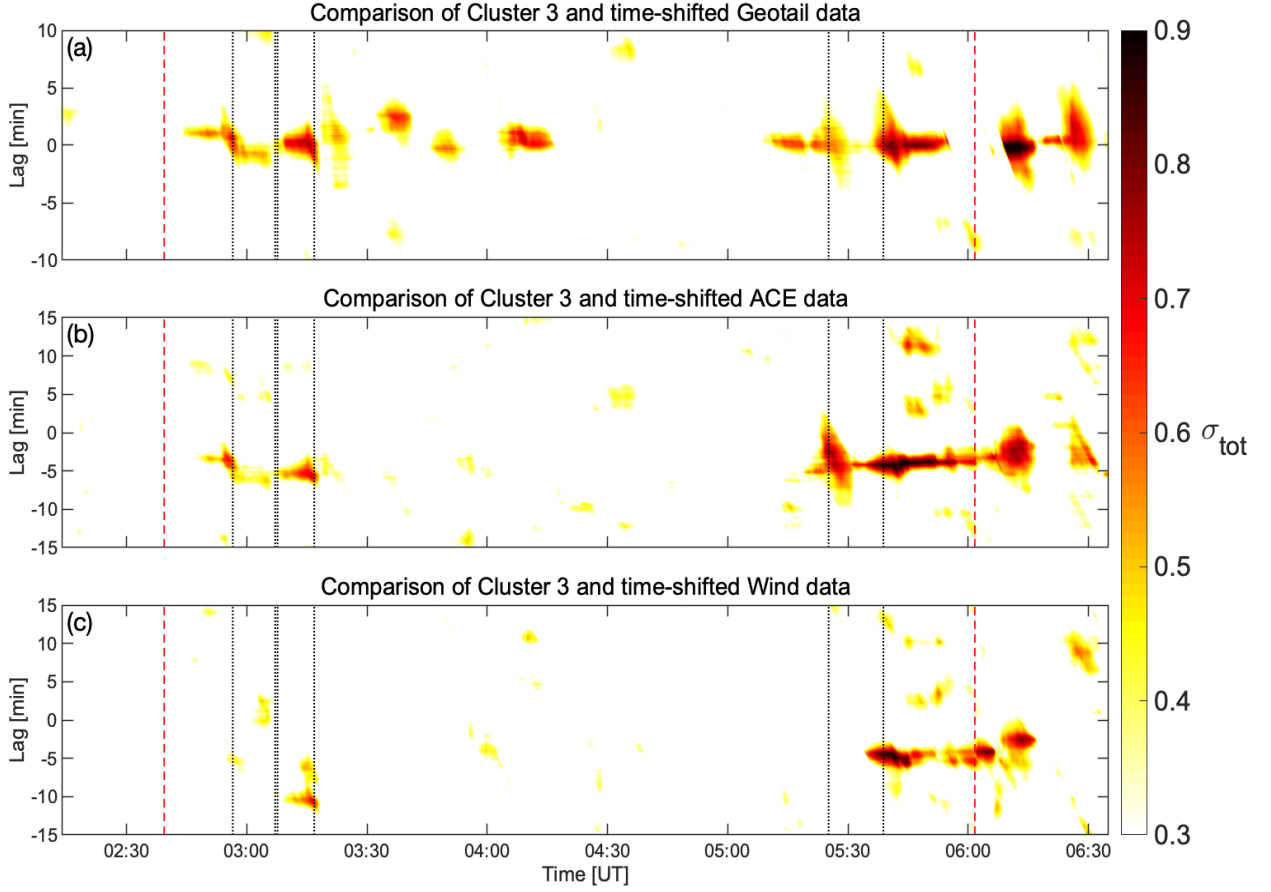


Figure 4. Total correlation between the magnetic field measurements at C3 and the other spacecraft. (a–c) σ_{tot} for C3 data correlated with time-shifted GT, ACE, and Wind data, respectively. Red vertical dashed lines indicate the shock and ICME leading edge, and black dotted lines are the boundaries given in Fig. 3a. Sub-intervals of C3 and GT data are compared to each other by taking a 10 min sub-interval of C3 data and the 20 min surrounding of corresponding (time-shifted) GT/ACE/Wind data. A sub-interval of C3 data, of which the observation time is given on the horizontal axis, is compared to a corresponding sub-interval of GT/ACE/Wind data, the values of σ_{tot} being computed by shifting the location of this sub-interval of GT/ACE/Wind data. The shift is defined as the lag. The lower boundary of the color bar, $\sigma_{tot} = 0.30$, is the lower quartile of the distribution of correlation maxima defined in the text.

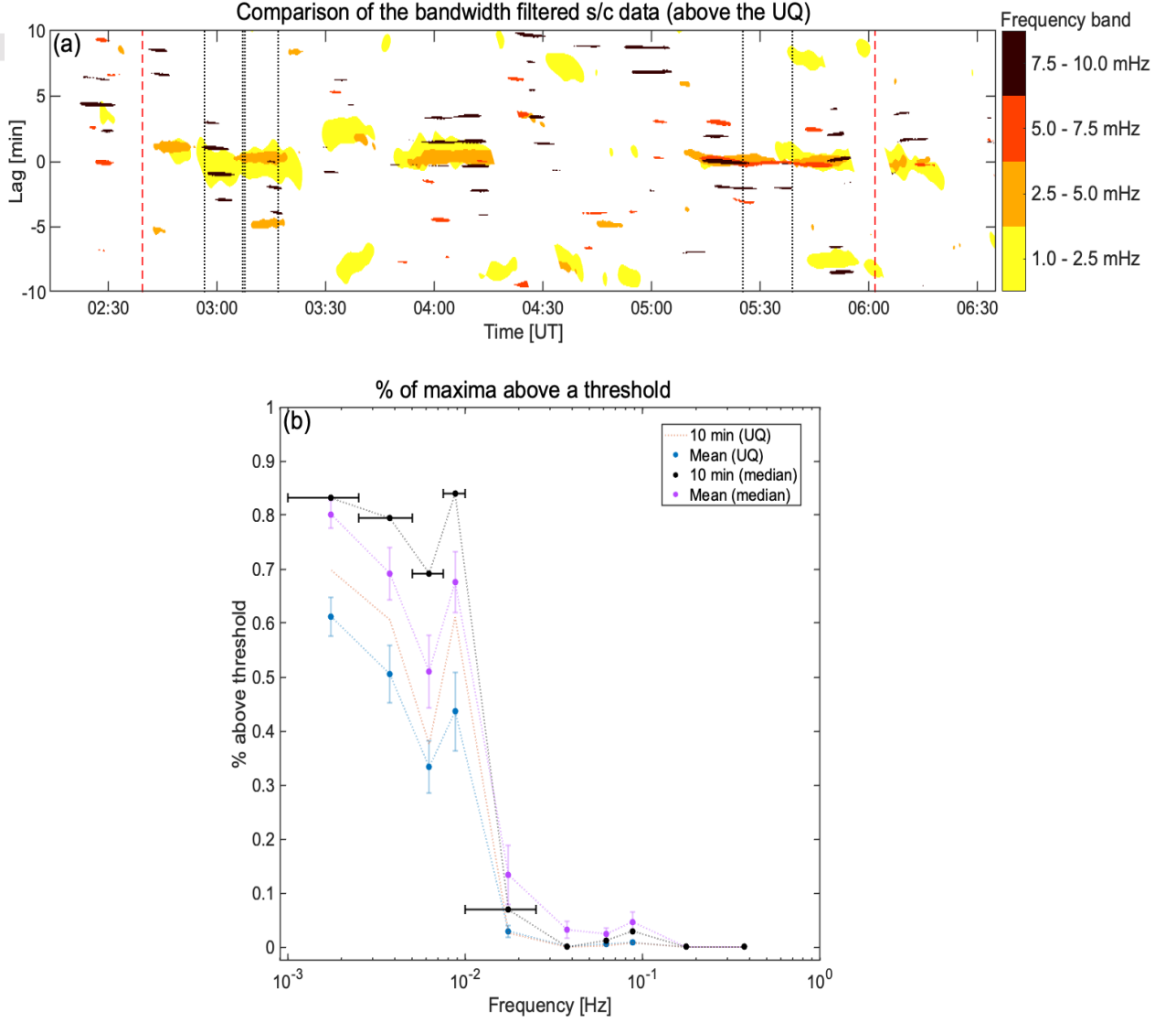


Figure 5. (a) Total correlation between the band-pass-filtered magnetic field data at C3 and GT during the ICME passage. Patches in the map show when the threshold of $\sigma_{tot} = 0.60$ is exceeded, and colors indicate the frequency bands investigated. The threshold is the upper quartile (UQ) of the distribution of correlation maxima defined in the text. (b) The percentage of σ_{tot} maxima as a function of bandwidth filtered spacecraft data. The percentages are computed for different interval lengths and different thresholds. The percentages are shown when 10 min C3 intervals were considered, and when the average of 5, 10, 20 and 30 min intervals were computed. The vertical error bars give the standard error of the mean. The thresholds are the median ($\sigma_{tot} = 0.48$) and UQ ($\sigma_{tot} = 0.60$) of the distribution of correlation maxima defined in the text. The black horizontal bars indicate the frequency bands used. The trend of the bands is also applied for the highest frequency bands but not shown due to all curves overlapping. ‘s/c’ refers to spacecraft.

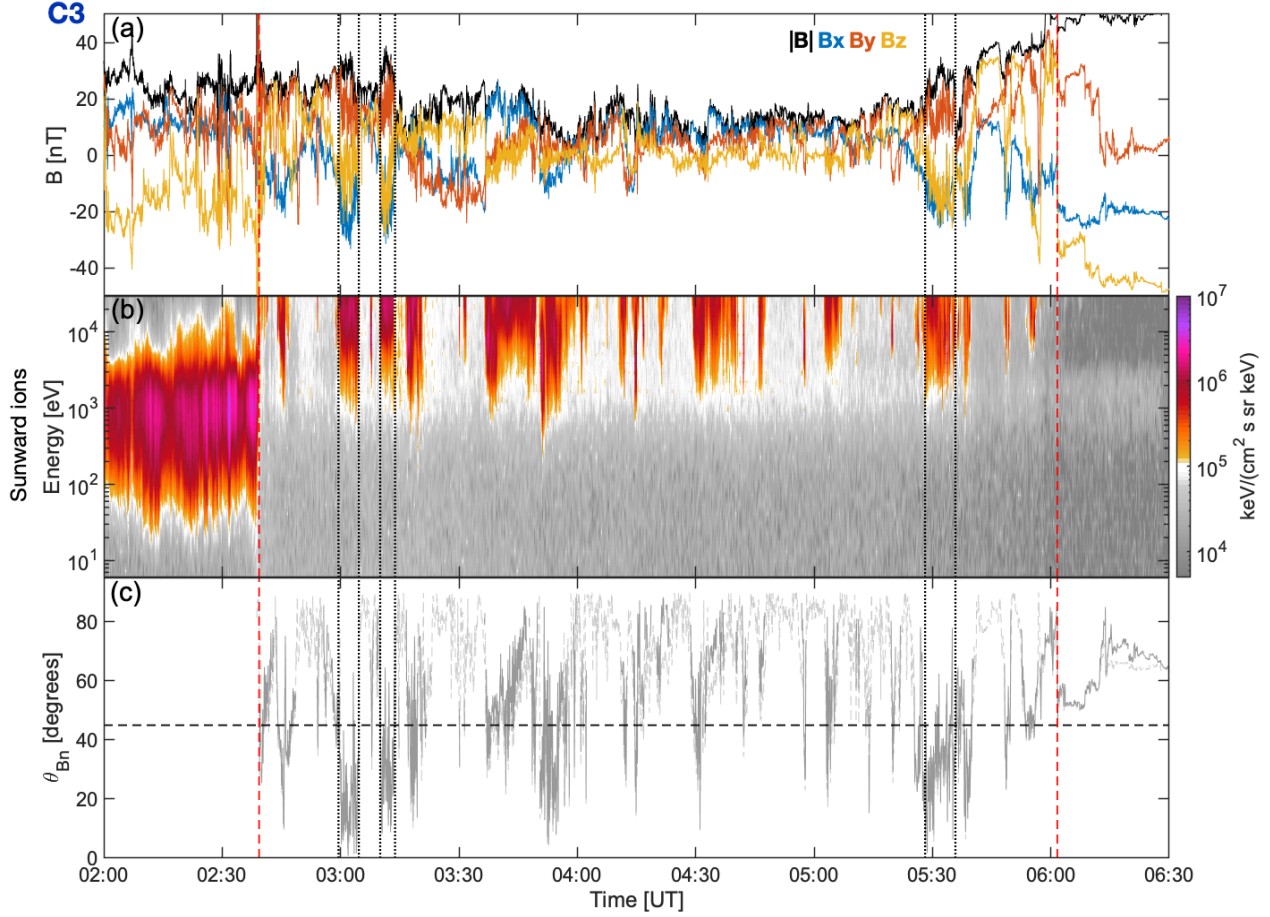


Figure 6. (a) C3 magnetic field measurements and (b) corresponding energy flux of sunward-traveling ions. (c) The estimated shock angle (θ_{bn}) of the Earth's bow shock when the magnetic field at C3 (solid gray) is extrapolated to the bow shock configuration according to Merka et al. (2005). The dashed gray curve indicates θ_{bn} when the path along the magnetic field direction given by C3 observations does not cross the bow shock due to the orientation of the magnetic field, and the radial path from the location of C3 to the center of the Earth is used instead. Black dotted vertical lines indicate the structure boundaries given in Fig. 3a.

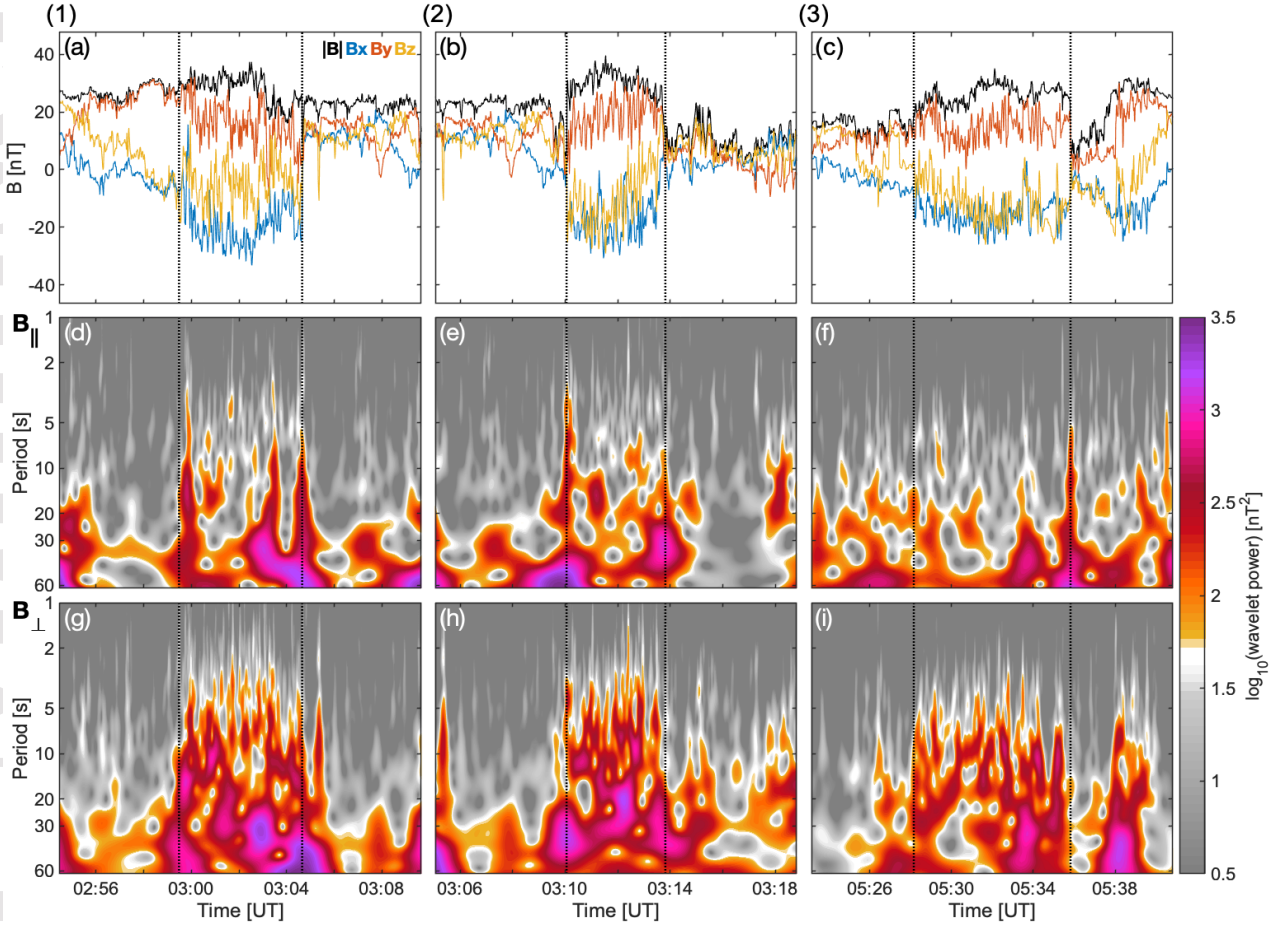


Figure 7. (a–c) C3 magnetic field measurements of structures (1)–(3), the structure boundaries given by black dotted vertical lines. (d–f) Wavelet power spectrum of magnetic field fluctuations parallel ($B_{||}$) and (g–i) perpendicular (B_{\perp}) to the mean field direction within the structures, for the time periods shown in panels (a–c). The power of B_{\perp} is the mean power of the two perpendicular components.

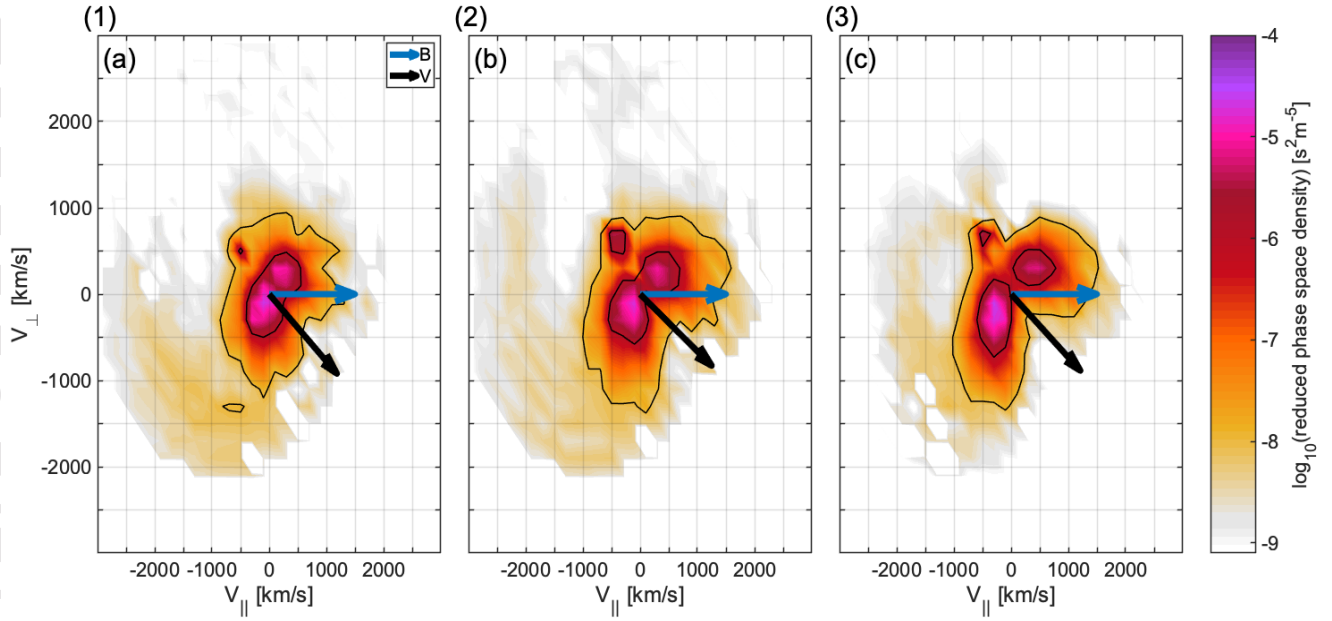


Figure 8. (a–c) Reduced ion velocity distribution functions observed during structures (1)–(3). The distributions are integrated over the second perpendicular velocity direction and color-coded according to the phase space density. Contours show \log_{10} values of -8 and -6. The horizontal and vertical axes are parallel and perpendicular to the magnetic field direction, which is shown by the blue arrows. The bulk plasma velocity is shown by the black arrow.

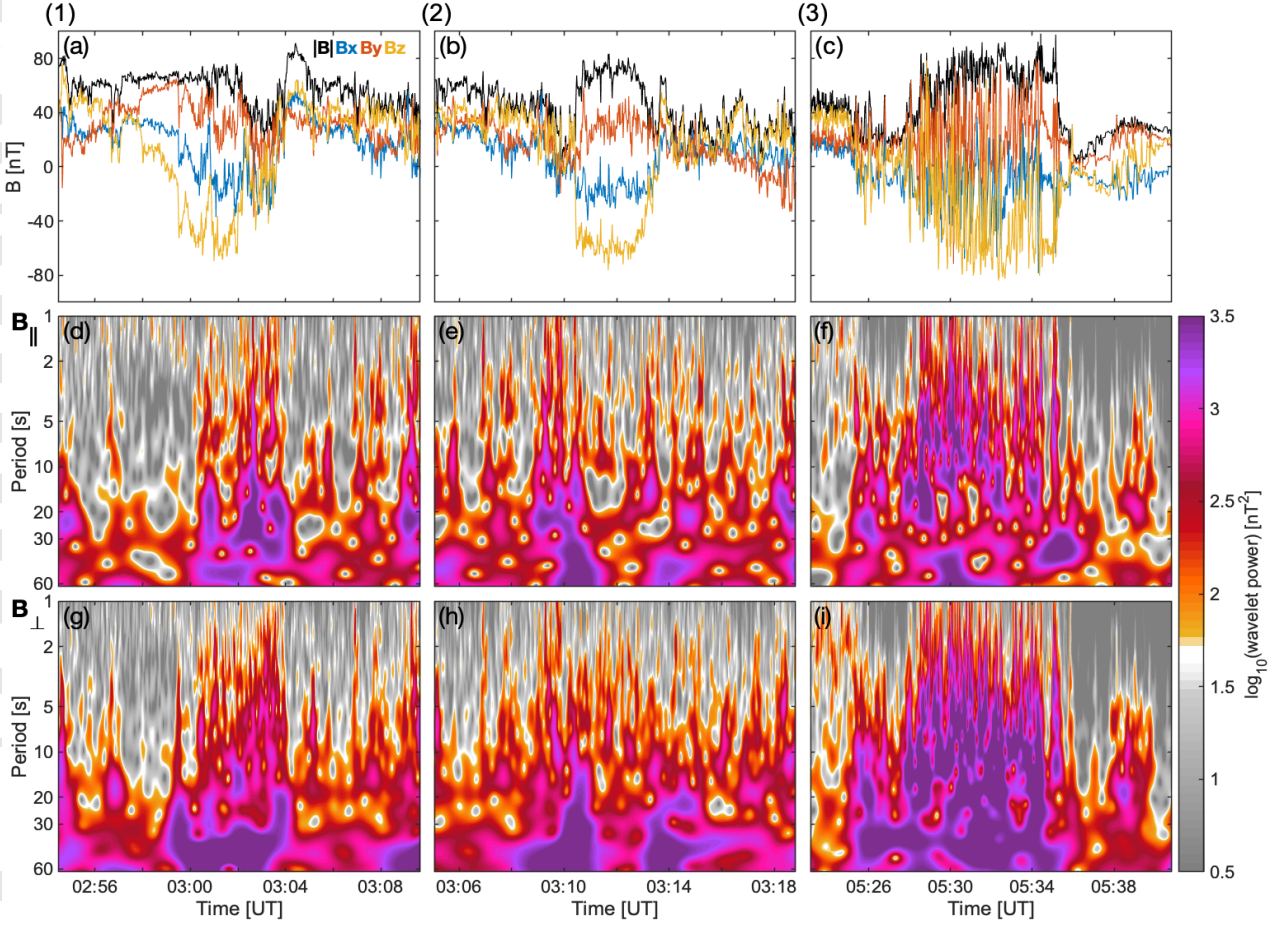


Figure 9. (a–c) GT magnetic field measurements of structures (1)–(3). (d–f) Wavelet power spectrum of magnetic field fluctuations parallel (B_{\parallel}) and (g–i) perpendicular (B_{\perp}) to the mean field direction within the structures at C3, for the time periods shown in Fig. 7a–c. The power of B_{\perp} is the mean power of the two perpendicular components.

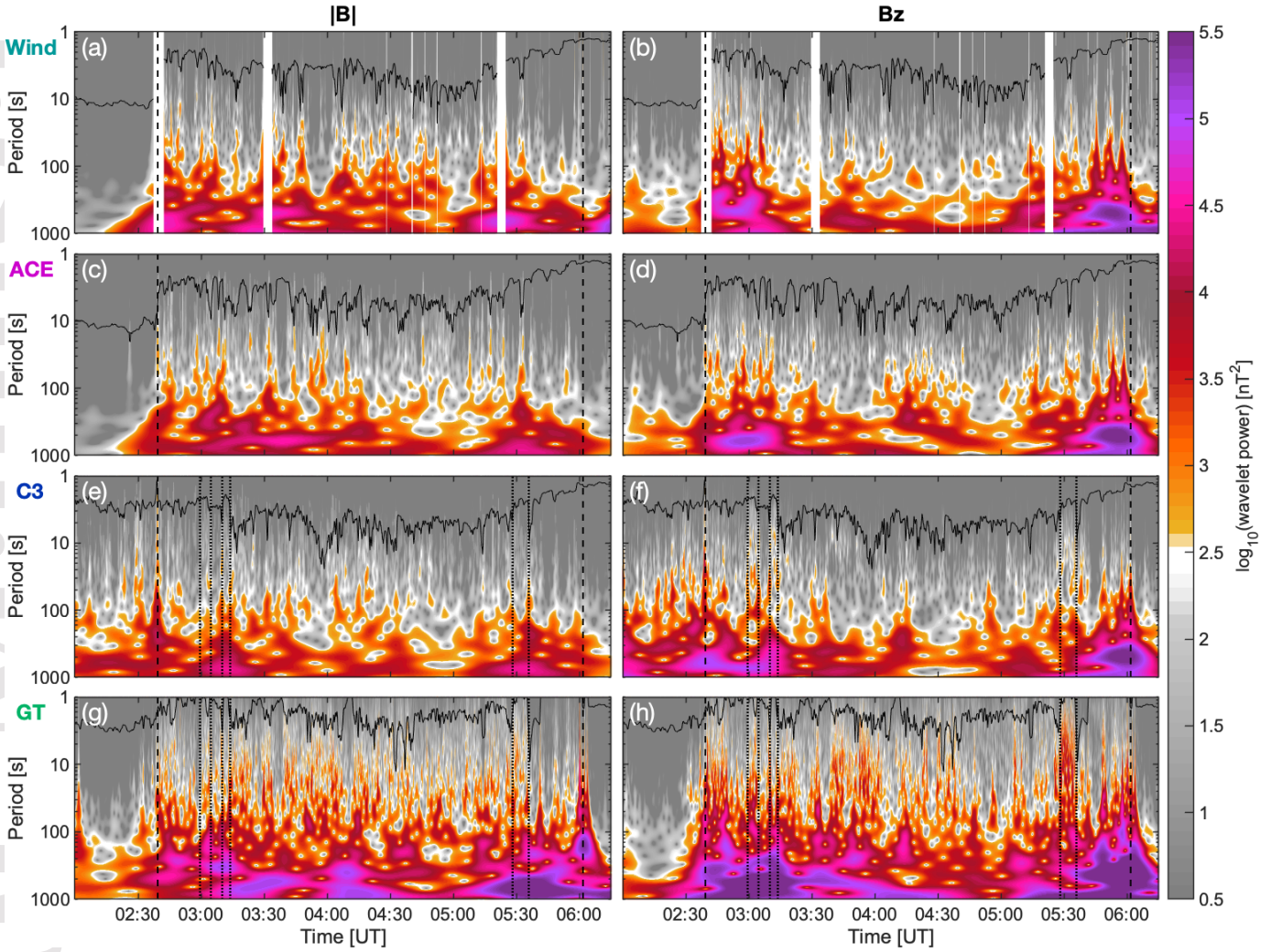


Figure 10. (a–h) Wavelet power spectrum of the magnetic field magnitude and GSE z component (B_z) during the ICME sheath passage at all spacecraft. The structure boundaries at C3 are marked by the black dotted vertical lines in panels (e–f) and extend to panels (g–h). The black dashed vertical lines give the ICME sheath boundaries. The solid black curves show the ion cyclotron period.

References

- 675
676 Ala-Lahti, M., Ruohotie, J., Good, S., Kilpua, E. K. J., & Lugaz, N. (2020, Sep). Spatial
677 Coherence of Interplanetary Coronal Mass Ejection Sheaths at 1 AU. *Journal of Geophysical Research (Space Physics)*, *125*(9), e28002. doi: 10.1029/2020JA028002
- 678 Alexander, R. A. (1990). A note on averaging correlations. *Bulletin of the Psychonomic Society*, *28*(4), 335–336. doi: 10.3758/BF03334037
- 680 Archer, M., Horbury, T. S., Lucek, E. A., Mazelle, C., Balogh, A., & Dandouras, I. (2005,
681 May). Size and shape of ULF waves in the terrestrial foreshock. *Journal of Geophysical Research (Space Physics)*, *110*(A5), A05208. doi: 10.1029/2004JA010791
- 682 Balogh, A., Dunlop, M. W., Cowley, S. W. H., Southwood, D. J., Thomlinson, J. G.,
683 Glassmeier, K. H., ... Kivelson, M. G. (1997, Jan). The Cluster Magnetic Field Investigation. *Space Science Reviews*, *79*, 65–91. doi: 10.1023/A:1004970907748
- 684 Bisi, M. M., Breen, A. R., Jackson, B. V., Fallows, R. A., Walsh, A. P., Mikić, Z., ... Pintér,
685 B. (2010, Aug). From the Sun to the Earth: The 13 May 2005 Coronal Mass Ejection.
686 *Solar Physics*, *265*(1-2), 49–127. doi: 10.1007/s11207-010-9602-8
- 687 Blanco-Cano, X., Kajdić, P., Aguilar-Rodríguez, E., Russell, C. T., Jian, L. K., & Luhmann,
688 J. G. (2016, Feb). Interplanetary shocks and foreshocks observed by STEREO during
689 2007–2010. *Journal of Geophysical Research (Space Physics)*, *121*(2), 992–1008. doi:
690 10.1002/2015JA021645
- 691 Blanco-Cano, X., Omidi, N., & Russell, C. T. (2006, Oct). Macrostructure of collisionless
692 bow shocks: 2. ULF waves in the foreshock and magnetosheath. *Journal of Geophysical Research (Space Physics)*, *111*(A10), A10205. doi: 10.1029/2005JA011421
- 693 Blum, L. W., Koval, A., Richardson, I. G., Wilson, L. B., Malaspina, D., Greeley, A.,
694 & Jaynes, A. N. (2021, Jun). Prompt Response of the Dayside Magnetosphere to
695 Discrete Structures Within the Sheath Region of a Coronal Mass Ejection. *Geophysical Research Letters*, *48*(11), e92700. doi: 10.1029/2021GL092700
- 696 Boudouridis, A., Zesta, E., Lyons, L. R., Anderson, P. C., & Lummerzheim, D. (2005, May).
697 Enhanced solar wind geoeffectiveness after a sudden increase in dynamic pressure
698 during southward IMF orientation. *Journal of Geophysical Research (Space Physics)*,
699 *110*(A5), A05214. doi: 10.1029/2004JA010704
- 700 Burgess, D. (1997, Sep). What do we really know about upstream waves? *Advances in Space Research*, *20*(4-5), 673–682. doi: 10.1016/S0273-1177(97)00455-9
- 701 Burton, R. K., McPherron, R. L., & Russell, C. T. (1975, Nov). An empirical relationship
702 between interplanetary conditions and Dst. *Journal of Geophysical Research*, *80*(31),
703 4204. doi: 10.1029/JA080i031p04204
- 704 Chen, L.-J., Ng, J., Omelchenko, Y., & Wang, S. (2021, Jun). Magnetopause Reconnection
705 and Indents Induced by Foreshock Turbulence. *Geophysical Research Letters*, *48*(11),
706 e93029. doi: 10.1029/2021GL093029
- 707 Clausen, L. B. N., Yeoman, T. K., Fear, R. C., Behlke, R., Lucek, E. A., & Engebretson,
708 M. J. (2009, Jan). First simultaneous measurements of waves generated at the bow
709 shock in the solar wind, the magnetosphere and on the ground. *Annales Geophysicae*,
710 *27*(1), 357–371. doi: 10.5194/angeo-27-357-2009
- 711 Crooker, N. U. (2000, Aug). Solar and heliospheric geoeffective disturbances. *Journal of Atmospheric and Solar-Terrestrial Physics*, *62*(12), 1071–1085. doi: 10.1016/S1364-6826(00)00098-5
- 712 Dasso, S., Mandrini, C. H., Démoulin, P., & Luoni, M. L. (2006, Aug). A new model-
713 independent method to compute magnetic helicity in magnetic clouds. *Astronomy and Astrophysics*, *455*(1), 349–359. doi: 10.1051/0004-6361:20064806
- 714 Dasso, S., Mandrini, C. H., Schmieder, B., Cremades, H., Cid, C., Cerrato, Y., ... Poedts,
715 S. (2009, Feb). Linking two consecutive nonmerging magnetic clouds with their solar
716 sources. *Journal of Geophysical Research (Space Physics)*, *114*(A2), A02109. doi:
717 10.1029/2008JA013102
- 718 Dimmock, A. P., Rosenqvist, L., Hall, J. O., Viljanen, A., Yordanova, E., Honkonen, I., ...
719 Sjöberg, E. C. (2019, Jul). The GIC and Geomagnetic Response Over Fennoscandia

- 729 to the 7-8 September 2017 Geomagnetic Storm. *Space Weather*, 17(7), 989-1010. doi:
730 10.1029/2018SW002132
- 731 Eastwood, J. P., Balogh, A., Lucek, E. A., Mazelle, C., & Dandouras, I. (2003, Jul). On the
732 existence of Alfvén waves in the terrestrial foreshock. *Annales Geophysicae*, 21(7),
733 1457-1465. doi: 10.5194/angeo-21-1457-2003
- 734 Eastwood, J. P., Balogh, A., Lucek, E. A., Mazelle, C., & Dandouras, I. (2005b, Nov).
735 Quasi-monochromatic ULF foreshock waves as observed by the four-spacecraft Cluster
736 mission: 1. Statistical properties. *Journal of Geophysical Research (Space Physics)*,
737 110(A11), A11219. doi: 10.1029/2004JA010617
- 738 Eastwood, J. P., Lucek, E. A., Mazelle, C., Meziane, K., Narita, Y., Pickett, J., & Treumann,
739 R. A. (2005a, Jun). The Foreshock. *Space Science Reviews*, 118(1-4), 41-94. doi:
740 10.1007/s11214-005-3824-3
- 741 Fox, N. J., Velli, M. C., Bale, S. D., Decker, R., Driesman, A., Howard, R. A., ... Szabo,
742 A. (2016, Nov). The Solar Probe Plus Mission: Humanity's First Visit to Our Star.
743 *Space Science Reviews*, 204(1-4), 7-48. doi: 10.1007/s11214-015-0211-6
- 744 Francia, P., Regi, M., De Lauretis, M., Villante, U., & Pilipenko, V. A. (2012, Jan). A
745 case study of upstream wave transmission to the ground at polar and low latitudes.
746 *Journal of Geophysical Research (Space Physics)*, 117(A1), A01210. doi: 10.1029/
747 2011JA016751
- 748 Fuselier, S. A. (1995, Jan). Ion distributions in the Earth's foreshock upstream from the
749 bow shock. *Advances in Space Research*, 15(8-9), 43-52. doi: 10.1016/0273-1177(94)
750 00083-D
- 751 Gary, S. P. (1985, Jan). Electromagnetic ion beam instabilities - Hot beams at interplanetary
752 shocks. *Astrophysical Journal*, 288, 342-352. doi: 10.1086/162797
- 753 Gary, S. P. (1991, May). Electromagnetic Ion / Ion Instabilities and Their Consequences
754 in Space Plasmas - a Review. *Space Science Reviews*, 56(3-4), 373-415. doi: 10.1007/
755 BF00196632
- 756 Gonzalez, W. D., Echer, E., Tsurutani, B. T., Clúa de Gonzalez, A. L., & Dal Lago, A.
757 (2011, Jan). Interplanetary Origin of Intense, Superintense and Extreme Geomagnetic
758 Storms. *Space Science Reviews*, 158(1), 69-89. doi: 10.1007/s11214-010-9715-2
- 759 Gonzalez, W. D., Tsurutani, B. T., & Clúa de Gonzalez, A. L. (1999, Apr). Interplanetary
760 origin of geomagnetic storms. *Space Science Reviews*, 88, 529-562. doi: 10.1023/A:
761 1005160129098
- 762 Good, S. W., Ala-Lahti, M., Palmerio, E., Kilpua, E. K. J., & Osmane, A. (2020, Apr).
763 Radial Evolution of Magnetic Field Fluctuations in an Interplanetary Coronal Mass
764 Ejection Sheath. *The Astrophysical Journal*, 893(2), 110. doi: 10.3847/1538-4357/
765 ab7fa2
- 766 Good, S. W., Forsyth, R. J., Eastwood, J. P., & Möstl, C. (2018, Mar). Correlation of
767 ICME Magnetic Fields at Radially Aligned Spacecraft. *Solar Physics*, 293(3), 52.
768 doi: 10.1007/s11207-018-1264-y
- 769 Good, S. W., Kilpua, E. K. J., LaMoury, A. T., Forsyth, R. J., Eastwood, J. P., & Möstl, C.
770 (2019, Jul). Self-Similarity of ICME Flux Ropes: Observations by Radially Aligned
771 Spacecraft in the Inner Heliosphere. *Journal of Geophysical Research (Space Physics)*,
772 124(7), 4960-4982. doi: 10.1029/2019JA026475
- 773 Gosling, J. T., & McComas, D. J. (1987, Apr). Field line draping about fast coronal mass
774 ejecta: A source of strong out-of-the-ecliptic interplanetary magnetic fields. *Geophys-
775 ical Research Letters*, 14(4), 355-358. doi: 10.1029/GL014i004p00355
- 776 Greenstadt, E. W., Green, I. M., Inouye, G. T., Hundhausen, A. J., Bame, S. J., & Strong,
777 I. B. (1968, Jan). Correlated magnetic field and plasma observations of the Earth's bow
778 shock. *Journal of Geophysical Research*, 73(1), 51. doi: 10.1029/JA073i001p00051
- 779 Hietala, H., Kilpua, E. K. J., Turner, D. L., & Angelopoulos, V. (2014, Apr). Depleting
780 effects of ICME-driven sheath regions on the outer electron radiation belt. *Geophysical
781 Research Letters*, 41(7), 2258-2265. doi: 10.1002/2014GL059551
- 782 Hobara, Y., Walker, S. N., Balikhin, M., Pokhotelov, O. A., Dunlop, M., Nilsson, H., &
783 Rème, H. (2007, Jul). Characteristics of terrestrial foreshock ULF waves: Cluster

- 784 observations. *Journal of Geophysical Research (Space Physics)*, 112(A7), A07202.
785 doi: 10.1029/2006JA012142
- 786 Hoppe, M. M., & Russell, C. T. (1982, Jan). Particle acceleration at planetary bow shock
787 waves. *Nature*, 295(5844), 41-42. doi: 10.1038/295041a0
- 788 Hsieh, W. C., & Shue, J. H. (2013, Jul). Dependence of the oblique propagation of ULF
789 foreshock waves on solar wind parameters. *Journal of Geophysical Research (Space
790 Physics)*, 118(7), 4151-4160. doi: 10.1002/jgra.50225
- 791 Huttunen, K. E. J., Kilpua, S. P., Pulkkinen, A., Viljanen, A., & Tanskanen, E. (2008,
792 Oct). Solar wind drivers of large geomagnetically induced currents during the solar
793 cycle 23. *Space Weather*, 6(10), S10002. doi: 10.1029/2007SW000374
- 794 Huttunen, K. E. J., & Koskinen, H. E. J. (2004, May). Importance of post-shock streams and
795 sheath region as drivers of intense magnetospheric storms and high-latitude activity.
796 *Annales Geophysicae*, 22(5), 1729-1738. doi: 10.5194/angeo-22-1729-2004
- 797 Huttunen, K. E. J., Koskinen, H. E. J., & Schwenn, R. (2002, Jul). Variability of magne-
798 toospheric storms driven by different solar wind perturbations. *Journal of Geophysical
799 Research (Space Physics)*, 107(A7), 1121. doi: 10.1029/2001JA900171
- 800 Janvier, M., Winslow, R. M., Good, S., Bonhomme, E., Démoulin, P., Dasso, S., ...
801 Boakes, P. D. (2019, Feb). Generic Magnetic Field Intensity Profiles of Interplan-
802 etary Coronal Mass Ejections at Mercury, Venus, and Earth From Superposed Epoch
803 Analyses. *Journal of Geophysical Research (Space Physics)*, 124(2), 812-836. doi:
804 10.1029/2018JA025949
- 805 Jones, G. H., Rees, A., Balogh, A., & Forsyth, R. J. (2002, Jun). The draping of heliospheric
806 magnetic fields upstream of coronal mass ejecta. *Geophysical Research Letters*, 29(11),
807 1520. doi: 10.1029/2001GL014110
- 808 Kajdič, P., Blanco-Cano, X., Omid, N., Rojas-Castillo, D., Sibeck, D. G., & Billing-
809 ham, L. (2017, Sep). Traveling Foreshocks and Transient Foreshock Phenom-
810 ena. *Journal of Geophysical Research (Space Physics)*, 122(9), 9148-9168. doi:
811 10.1002/2017JA023901
- 812 Kajdič, P., Preisser, L., Blanco-Cano, X., Burgess, D., & Trotta, D. (2019, Apr). First
813 Observations of Irregular Surface of Interplanetary Shocks at Ion Scales by Cluster.
814 *The Astrophysical Journal Letters*, 874(2), L13. doi: 10.3847/2041-8213/ab0e84
- 815 Kalliokoski, M. M. H., Kilpua, E. K. J., Osmane, A., Turner, D. L., Jaynes, A. N., Turc,
816 L., ... Palmroth, M. (2020, Jun). Outer radiation belt and inner magnetospheric
817 response to sheath regions of coronal mass ejections: a statistical analysis. *Annales
818 Geophysicae*, 38(3), 683-701. doi: 10.5194/angeo-38-683-2020
- 819 Kaymaz, Z., & Siscoe, G. (2006, Dec). Field-Line Draping Around ICMEs. *Solar Physics*,
820 239(1-2), 437-448. doi: 10.1007/s11207-006-0308-x
- 821 Kempf, Y., Pokhotelov, D., Gutynska, O., Wilson, I., Lynn B., Walsh, B. M., von Althaus,
822 S., ... Palmroth, M. (2015, May). Ion distributions in the Earth's foreshock: Hybrid-
823 Vlasov simulation and THEMIS observations. *Journal of Geophysical Research (Space
824 Physics)*, 120(5), 3684-3701. doi: 10.1002/2014JA020519
- 825 Kilpua, E. K. J., Balogh, A., von Steiger, R., & Liu, Y. D. (2017a, Nov). Geoeffective
826 Properties of Solar Transients and Stream Interaction Regions. *Space Science Reviews*,
827 212(3-4), 1271-1314. doi: 10.1007/s11214-017-0411-3
- 828 Kilpua, E. K. J., Fontaine, D., Moissard, C., Ala-Lahti, M., Palmerio, E., Yordanova, E., ...
829 Turc, L. (2019, Aug). Solar Wind Properties and Geospace Impact of Coronal Mass
830 Ejection-Driven Sheath Regions: Variation and Driver Dependence. *Space Weather*,
831 17(8), 1257-1280. doi: 10.1029/2019SW002217
- 832 Kilpua, E. K. J., Hietala, H., Koskinen, H. E. J., Fontaine, D., & Turc, L. (2013, Sep).
833 Magnetic field and dynamic pressure ULF fluctuations in coronal-mass-ejection-driven
834 sheath regions. *Annales Geophysicae*, 31(9), 1559-1567. doi: 10.5194/angeo-31-1559-
835 -2013
- 836 Kilpua, E. K. J., Koskinen, H. E. J., & Pulkkinen, T. I. (2017b, Nov). Coronal mass
837 ejections and their sheath regions in interplanetary space. *Living Reviews in Solar
838 Physics*, 14(1), 5. doi: 10.1007/s41116-017-0009-6

- 839 Kis, A., Scholer, M., Klecker, B., Möbius, E., Lucek, E. A., Rème, H., ... Kucharek, H.
840 (2004, Oct). Multi-spacecraft observations of diffuse ions upstream of Earth's bow
841 shock. *Geophysical Research Letters*, *31*(20), L20801. doi: 10.1029/2004GL020759
- 842 Knipp, D., Kilcommons, L., Hunt, L., Mlynczak, M., Pilipenko, V., Bowman, B., ...
843 Drake, K. (2013, Apr). Thermospheric damping response to sheath-enhanced geospace
844 storms. *Geophysical Research Letters*, *40*(7), 1263-1267. doi: 10.1002/grl.50197
- 845 Kokubun, S., Yamamoto, T., Acuña, M. H., Hayashi, K., Shiokawa, K., & Kawano, H.
846 (1994, Jan). The GEOTAIL Magnetic Field Experiment. *Journal of Geomagnetism
847 and Geoelectricity*, *46*(1), 7-21. doi: 10.5636/jgg.46.7
- 848 Lavraud, B., Ruffenach, A., Rouillard, A. P., Kajdic, P., Manchester, W. B., & Lugaz,
849 N. (2014, Jan). Geo-effectiveness and radial dependence of magnetic cloud erosion
850 by magnetic reconnection. *Journal of Geophysical Research (Space Physics)*, *119*(1),
851 26-35. doi: 10.1002/2013JA019154
- 852 Lepping, R. P., Acuña, M. H., Burlaga, L. F., Farrell, W. M., Slavin, J. A., Schatten, K. H.,
853 ... Worley, E. M. (1995, Feb). The Wind Magnetic Field Investigation. *Space Science
854 Reviews*, *71*, 207-229. doi: 10.1007/BF00751330
- 855 Lin, Y., & Wang, X. Y. (2005, Dec). Three-dimensional global hybrid simulation of day-
856 side dynamics associated with the quasi-parallel bow shock. *Journal of Geophysical
857 Research (Space Physics)*, *110*(A12), A12216. doi: 10.1029/2005JA011243
- 858 Lindsay, G. M., Russell, C. T., & Luhmann, J. G. (1995, Sep). Coronal mass ejection and
859 stream interaction region characteristics and their potential geomagnetic effectiveness.
860 *Journal of Geophysical Research*, *100*(A9), 16999-17014. doi: 10.1029/95JA00525
- 861 Lugaz, N., Farrugia, C. J., Winslow, R. M., Al-Haddad, N., Galvin, A. B., Nieves-
862 Chinchilla, T., ... Janvier, M. (2018, Sep). On the Spatial Coherence of Magnetic
863 Ejecta: Measurements of Coronal Mass Ejections by Multiple Spacecraft Longitu-
864 dinally Separated by 0.01 au. *The Astrophysical Journal Letters*, *864*(1), L7. doi:
865 10.3847/2041-8213/aad9f4
- 866 Lugaz, N., Farrugia, C. J., Winslow, R. M., Al-Haddad, N., Kilpua, E. K. J., & Riley,
867 P. (2016, Nov). Factors affecting the geoeffectiveness of shocks and sheaths at 1
868 AU. *Journal of Geophysical Research (Space Physics)*, *121*(11), 10,861-10,879. doi:
869 10.1002/2016JA023100
- 870 Lugaz, N., Winslow, R. M., & Farrugia, C. J. (2020, Jan). Evolution of a Long-Duration
871 Coronal Mass Ejection and Its Sheath Region Between Mercury and Earth on 9-14
872 July 2013. *Journal of Geophysical Research (Space Physics)*, *125*(1), e27213. doi:
873 10.1029/2019JA027213
- 874 Luhmann, J. G., Gopalswamy, N., Jian, L. K., & Lugaz, N. (2020, Apr). ICME Evolution
875 in the Inner Heliosphere. *Solar Physics*, *295*(4), 61. doi: 10.1007/s11207-020-01624-0
- 876 Manchester, W. B., Kilpua, E. K. J., Liu, Y. D., Lugaz, N., Riley, P., Török, T., & Vršnak,
877 B. (2017, Nov). The Physical Processes of CME/ICME Evolution. *Space Science
878 Reviews*, *212*(3-4), 1159-1219. doi: 10.1007/s11214-017-0394-0
- 879 Manchester, W. B., Kozyra, J. U., Lepri, S. T., & Lavraud, B. (2014, Jul). Simulation of
880 magnetic cloud erosion during propagation. *Journal of Geophysical Research (Space
881 Physics)*, *119*(7), 5449-5464. doi: 10.1002/2014JA019882
- 882 Mazelle, C., Meziane, K., Le Quéau, D., Wilber, M., Eastwood, J. P., Rème, H., ... Balogh,
883 A. (2003, Oct). Production of gyrating ions from nonlinear wave-particle interaction
884 upstream from the Earth's bow shock: A case study from Cluster-CIS. *Planetary and
885 Space Science*, *51*(12), 785-795. doi: 10.1016/j.pss.2003.05.002
- 886 McComas, D. J., Bame, S. J., Barker, P., Feldman, W. C., Phillips, J. L., Riley, P., &
887 Griffée, J. W. (1998, Jul). Solar Wind Electron Proton Alpha Monitor (SWEPAM)
888 for the Advanced Composition Explorer. *Space Science Reviews*, *86*, 563-612. doi:
889 10.1023/A:1005040232597
- 890 McComas, D. J., Gosling, J. T., Bame, S. J., Smith, E. J., & Cane, H. V. (1989, Feb). A test
891 of magnetic field draping induced B_z perturbations ahead of fast coronal mass ejecta.
892 *Journal of Geophysical Research*, *94*(A2), 1465-1471. doi: 10.1029/JA094iA02p01465
- 893 Meng, X., Tsurutani, B. T., & Mannucci, A. J. (2019, Jun). The Solar and Inter-

- 894 planetary Causes of Superstorms (Minimum Dst \leq -250 nT) During the Space
 895 Age. *Journal of Geophysical Research (Space Physics)*, *124*(6), 3926-3948. doi:
 896 10.1029/2018JA026425
- 897 Merka, J., Szabo, A., Slavin, J. A., & Peredo, M. (2005, Apr). Three-dimensional position
 898 and shape of the bow shock and their variation with upstream Mach numbers and
 899 interplanetary magnetic field orientation. *Journal of Geophysical Research (Space*
 900 *Physics)*, *110*(A4), A04202. doi: 10.1029/2004JA010944
- 901 Moissard, C., Fontaine, D., & Savoini, P. (2019, Nov). A Study of Fluctuations in Magnetic
 902 Cloud-Driven Sheaths. *Journal of Geophysical Research (Space Physics)*, *124*(11),
 903 8208-8226. doi: 10.1029/2019JA026952
- 904 Mukai, T., Machida, S., Saito, Y., Hirahara, M., Terasawa, T., Kaya, N., ... Nishida, A.
 905 (1994, Jan). The Low Energy Particle (LEP) Experiment onboard the GEOTAIL
 906 Satellite. *Journal of Geomagnetism and Geoelectricity*, *46*(8), 669-692. doi: 10.5636/
 907 jgg.46.669
- 908 Müller, D., Marsden, R. G., St. Cyr, O. C., & Gilbert, H. R. (2013, Jul). Solar Orbiter
 909 . Exploring the Sun-Heliosphere Connection. *Solar Physics*, *285*(1-2), 25-70. doi:
 910 10.1007/s11207-012-0085-7
- 911 Nakagawa, T., Nishida, A., & Saito, T. (1989, Sep). Planar magnetic structures in the
 912 solar wind. *Journal of Geophysical Research*, *94*(A9), 11761-11775. doi: 10.1029/
 913 JA094iA09p11761
- 914 Nykyri, K., Bengtson, M., Angelopoulos, V., Nishimura, Y., & Wing, S. (2019, Jun). Can
 915 Enhanced Flux Loading by High-Speed Jets Lead to a Substorm? Multipoint Detec-
 916 tion of the Christmas Day Substorm Onset at 08:17 UT, 2015. *Journal of Geophysical*
 917 *Research (Space Physics)*, *124*(6), 4314-4340. doi: 10.1029/2018JA026357
- 918 Ogilvie, K. W., Chornay, D. J., Fritzenreiter, R. J., Hunsaker, F., Keller, J., Lobell, J., ...
 919 Gergin, E. (1995, Feb). SWE, A Comprehensive Plasma Instrument for the Wind
 920 Spacecraft. *Space Science Reviews*, *71*, 55-77. doi: 10.1007/BF00751326
- 921 Oliveira, D. M., & Samsonov, A. A. (2018, Jan). Geoeffectiveness of interplanetary shocks
 922 controlled by impact angles: A review. *Advances in Space Research*, *61*(1), 1-44. doi:
 923 10.1016/j.asr.2017.10.006
- 924 Olkin, I., & Pratt, J. W. (1958, Mar). Unbiased Estimation of Certain Correlation Coef-
 925 ficients. *The Annals of Mathematical Statistics*, *29*(1), 201-211. doi: 10.1214/aoms/
 926 1177706717
- 927 Omidi, N., Sibeck, D. G., & Blanco-Cano, X. (2009, Aug). Foreshock compressional
 928 boundary. *Journal of Geophysical Research (Space Physics)*, *114*(A8), A08205. doi:
 929 10.1029/2008JA013950
- 930 Palmerio, E., Kilpua, E. K. J., & Savani, N. P. (2016, Feb). Planar magnetic structures
 931 in coronal mass ejection-driven sheath regions. *Annales Geophysicae*, *34*(2), 313-322.
 932 doi: 10.5194/angeo-34-313-2016
- 933 Palmroth, M., Archer, M., Vainio, R., Hietala, H., Pfau-Kempf, Y., Hoilijoki, S., ... East-
 934 wood, J. P. (2015, Oct). ULF foreshock under radial IMF: THEMIS observations and
 935 global kinetic simulation Vlasiator results compared. *Journal of Geophysical Research*
 936 *(Space Physics)*, *120*(10), 8782-8798. doi: 10.1002/2015JA021526
- 937 Paschmann, G., & Daly, P. W. (1998, Jan). Analysis Methods for Multi-Spacecraft Data.
 938 ISSI Scientific Reports Series SR-001, ESA/ISSI, Vol. 1. ISBN 1608-280X, 1998. *ISSI*
 939 *Scientific Reports Series*, *1*.
- 940 Paschmann, G., Sckopke, N., Bame, S. J., Asbridge, J. R., Gosling, J. T., Russell, C. T., &
 941 Greenstadt, E. W. (1979, Mar). Association of low-frequency waves with suprathermal
 942 ions in the upstream solar wind. *Geophysical Research Letters*, *6*(3), 209-212. doi:
 943 10.1029/GL006i003p00209
- 944 Pfau-Kempf, Y., Hietala, H., Milan, S. E., Juusola, L., Hoilijoki, S., Ganse, U., ...
 945 Palmroth, M. (2016, Nov). Evidence for transient, local ion foreshocks caused by
 946 dayside magnetopause reconnection. *Annales Geophysicae*, *34*(11), 943-959. doi:
 947 10.5194/angeo-34-943-2016
- 948 Pitňa, A., Šafránková, J., Němeček, Z., Goncharov, O., Němec, F., Přeč, L., ... Zastenker,

- 949 G. N. (2016, Mar). Density Fluctuations Upstream and Downstream of Interplanetary
950 Shocks. *The Astrophysical Journal*, *819*(1), 41. doi: 10.3847/0004-637X/819/1/41
- 951 Pitňa, A., Šafránková, J., Němeček, Z., Ďurovcová, T., & Kis, A. (2021, Apr). Turbulence
952 Upstream and Downstream of Interplanetary Shocks. *Frontiers in Physics*, *8*, 654.
953 doi: 10.3389/fphy.2020.626768
- 954 Pulkkinen, T. I., Partamies, N., Huttunen, K. E. J., Reeves, G. D., & Koskinen, H. E. J.
955 (2007, Jan). Differences in geomagnetic storms driven by magnetic clouds and
956 ICME sheath regions. *Geophysical Research Letters*, *34*(2), L02105. doi: 10.1029/
957 2006GL027775
- 958 Rakhmanova, L., Riazantseva, M., Zastenker, G., & Šafránková, J. (2015, Sep). Modification
959 of small- and middle-scale solar wind structures by the bow shock and magnetosheath:
960 Correlation analysis. *Planetary and Space Science*, *115*, 12-18. doi: 10.1016/j.pss.2015
961 .03.003
- 962 Réme, H., Bosqued, J. M., Sauvaud, J. A., Cros, A., Dandouras, J., Aoustin, C., ... Balsiger,
963 H. (1997, Jan). The Cluster Ion Spectrometry (cis) Experiment. *Space Science
964 Reviews*, *79*, 303-350. doi: 10.1023/A:1004929816409
- 965 Rojas-Castillo, D., Blanco-Cano, X., Kajdič, P., & Omid, N. (2013, Feb). Foreshock
966 compressional boundaries observed by Cluster. *Journal of Geophysical Research (Space
967 Physics)*, *118*(2), 698-715. doi: 10.1029/2011JA017385
- 968 Ruffenach, A., Lavraud, B., Owens, M. J., Sauvaud, J. A., Savani, N. P., Rouillard, A. P.,
969 ... Galvin, A. B. (2012, Sep). Multispacecraft observation of magnetic cloud erosion
970 by magnetic reconnection during propagation. *Journal of Geophysical Research (Space
971 Physics)*, *117*(A9), A09101. doi: 10.1029/2012JA017624
- 972 Russell, C. T., Luhmann, J. G., Odera, T. J., & Stuart, W. F. (1983, Aug). The rate of
973 occurrence of dayside Pc 3,4 pulsations: The L-value dependence of the IMF cone angle
974 effect. *Geophysical Research Letters*, *10*(8), 663-666. doi: 10.1029/GL010i008p00663
- 975 Salman, T. M., Lugaz, N., Farrugia, C. J., Winslow, R. M., Jian, L. K., & Galvin, A. B.
976 (2020, Dec). Properties of the Sheath Regions of Coronal Mass Ejections with or
977 without Shocks from STEREO in situ Observations near 1 au. *The Astrophysical
978 Journal*, *904*(2), 177. doi: 10.3847/1538-4357/abbd5f
- 979 Scolini, C., Verbeke, C., Poedts, S., Chané, E., Pomoell, J., & Zuccarello, F. P. (2018,
980 Jun). Effect of the Initial Shape of Coronal Mass Ejections on 3-D MHD Simulations
981 and Geoeffectiveness Predictions. *Space Weather*, *16*(6), 754-771. doi: 10.1029/
982 2018SW001806
- 983 Shue, J. H., Song, P., Russell, C. T., Steinberg, J. T., Chao, J. K., Zastenker, G., ...
984 Kawano, H. (1998, Aug). Magnetopause location under extreme solar wind conditions.
985 *Journal of Geophysical Research*, *103*(A8), 17691-17700. doi: 10.1029/98JA01103
- 986 Smith, C. W., L'Heureux, J., Ness, N. F., Acuña, M. H., Burlaga, L. F., & Scheifele, J. (1998,
987 Jul). The ACE Magnetic Fields Experiment. *Space Science Reviews*, *86*, 613-632. doi:
988 10.1023/A:1005092216668
- 989 Takahashi, K., McPherron, R. L., & Terasawa, T. (1984, May). Dependence of the spectrum
990 of Pc 3-4 pulsations on the interplanetary magnetic field. *Journal of Geophysical
991 Research*, *89*(A5), 2770-2780. doi: 10.1029/JA089iA05p02770
- 992 Takahashi, K., Turc, L., Kilpua, E., Takahashi, N., Dimmock, A., Kajdic, P., ... Battarbee,
993 M. (2021, Feb). Propagation of Ultralow Frequency Waves from the Ion Foreshock into
994 the Magnetosphere During the Passage of a Magnetic Cloud. *Journal of Geophysical
995 Research (Space Physics)*, *126*(2), e28474. doi: 10.1029/2020JA028474
- 996 Tsurutani, B. T., Gonzalez, W. D., Tang, F., Akasofu, S. I., & Smith, E. J. (1988, Aug).
997 Origin of interplanetary southward magnetic fields responsible for major magnetic
998 storms near solar maximum (1978-1979). *Journal of Geophysical Research*, *93*(A8),
999 8519-8531. doi: 10.1029/JA093iA08p08519
- 1000 Tsurutani, B. T., Hajra, R., Echer, E., & Gjerloev, J. W. (2015, May). Extremely intense
1001 (SML \leq -2500 nT) substorms: isolated events that are externally triggered? *Annales
1002 Geophysicae*, *33*(5), 519-524. doi: 10.5194/angeo-33-519-2015
- 1003 Tsurutani, B. T., Lakhina, G. S., & Hajra, R. (2020, Feb). The physics of space

- 1004 weather/solar-terrestrial physics (STP): what we know now and what the current
 1005 and future challenges are. *Nonlinear Processes in Geophysics*, 27(1), 75-119. doi:
 1006 10.5194/npg-27-75-2020
- 1007 Tsurutani, B. T., Lakhina, G. S., Verkhoglyadova, O. P., Gonzalez, W. D., Echer, E., &
 1008 Guarnieri, F. L. (2011, Jan). A review of interplanetary discontinuities and their
 1009 geomagnetic effects. *Journal of Atmospheric and Solar-Terrestrial Physics*, 73(1),
 1010 5-19. doi: 10.1016/j.jastp.2010.04.001
- 1011 Turc, L., Fontaine, D., Escoubet, C. P., Kilpua, E. K. J., & Dimmock, A. P. (2017, Mar).
 1012 Statistical study of the alteration of the magnetic structure of magnetic clouds in the
 1013 Earth's magnetosheath. *Journal of Geophysical Research (Space Physics)*, 122(3),
 1014 2956-2972. doi: 10.1002/2016JA023654
- 1015 Turc, L., Fontaine, D., Savoini, P., & Kilpua, E. K. J. (2014, Oct). Magnetic clouds'
 1016 structure in the magnetosheath as observed by Cluster and Geotail: four case studies.
 1017 *Annales Geophysicae*, 32(10), 1247-1261. doi: 10.5194/angeo-32-1247-2014
- 1018 Turc, L., Ganse, U., Pfau-Kempf, Y., Hoilijoki, S., Battarbee, M., Juusola, L., ... Palm-
 1019 roth, M. (2018, Jul). Foreshock Properties at Typical and Enhanced Interplanetary
 1020 Magnetic Field Strengths: Results From Hybrid-Vlasov Simulations. *Journal of Geo-
 1021 physical Research (Space Physics)*, 123(7), 5476-5493. doi: 10.1029/2018JA025466
- 1022 Turc, L., Roberts, O. W., Archer, M. O., Palmroth, M., Battarbee, M., Brito, T., ... Dan-
 1023 douras, I. (2019, Nov). First Observations of the Disruption of the Earth's Foreshock
 1024 Wave Field During Magnetic Clouds. *Geophysical Research Letters*, 46(22), 12,644-
 1025 12,653. doi: 10.1029/2019GL084437
- 1026 Turner, D. L., Kilpua, E. K. J., Hietala, H., Claudepierre, S. G., O'Brien, T. P., Fennell,
 1027 J. F., ... Reeves, G. D. (2019, Feb). The Response of Earth's Electron Radiation
 1028 Belts to Geomagnetic Storms: Statistics From the Van Allen Probes Era Including Ef-
 1029 fects From Different Storm Drivers. *Journal of Geophysical Research (Space Physics)*,
 1030 124(2), 1013-1034. doi: 10.1029/2018JA026066
- 1031 Villante, U., De Paulis, C., & Francia, P. (2011, Jun). The transmission of upstream waves
 1032 to the magnetosphere: An analysis at widely separated ground stations. *Journal of
 1033 Geophysical Research (Space Physics)*, 116(A6), A06219. doi: 10.1029/2010JA016263
- 1034 Wilson, L. B. (2016, Feb). Low Frequency Waves at and Upstream of Collisionless Shocks.
 1035 *Washington DC American Geophysical Union Geophysical Monograph Series*, 216,
 1036 269-291. doi: 10.1002/9781119055006.ch16
- 1037 Winslow, R. M., Lugaz, N., Scolini, C., & Galvin, A. B. (2021, Aug). First Simultaneous In
 1038 Situ Measurements of a Coronal Mass Ejection by Parker Solar Probe and STEREO-A.
 1039 *The Astrophysical Journal*, 916(2), 94. doi: 10.3847/1538-4357/ac0821
- 1040 Yermolaev, Y. I., Lodkina, I. G., Nikolaeva, N. S., Yermolaev, M. Y., Riazantseva, M. O., &
 1041 Rakhmanova, L. S. (2018, Nov). Statistic study of the geoeffectiveness of compression
 1042 regions CIRs and Sheaths. *Journal of Atmospheric and Solar-Terrestrial Physics*, 180,
 1043 52-59. doi: 10.1016/j.jastp.2018.01.027
- 1044 Yermolaev, Y. I., Nikolaeva, N. S., Lodkina, I. G., & Yermolaev, M. Y. (2012, May).
 1045 Geoeffectiveness and efficiency of CIR, sheath, and ICME in generation of magnetic
 1046 storms. *Journal of Geophysical Research (Space Physics)*, 117, A00L07. doi: 10.1029/
 1047 2011JA017139
- 1048 Yurchyshyn, V., Liu, C., Abramenko, V., & Krall, J. (2006, Dec). The May 13, 2005
 1049 Eruption: Observations, Data Analysis and Interpretation. *Solar Physics*, 239(1-2),
 1050 317-335. doi: 10.1007/s11207-006-0177-3
- 1051 Zank, G. P., Nakanotani, M., Zhao, L. L., Du, S., Adhikari, L., Che, H., & le Roux, J. A.
 1052 (2021, Jun). Flux Ropes, Turbulence, and Collisionless Perpendicular Shock Waves:
 1053 High Plasma Beta Case. *The Astrophysical Journal*, 913(2), 127. doi: 10.3847/
 1054 1538-4357/abf7c8
- 1055 Zhou, X., & Tsurutani, B. T. (2001, Sep). Interplanetary shock triggering of nightside
 1056 geomagnetic activity: Substorms, pseudobreakups, and quiescent events. *Journal of
 1057 Geophysical Research*, 106(A9), 18957-18968. doi: 10.1029/2000JA003028